Aerodynamic Design of Moveable Inlet Guide Vanes for Active Control of Rotating Stall

by

Peter D. Silkowski

B.S. Aeronautical and Astronautical Engineering, University of Illinois (1987)

SUBMITTED IN PARTIAL FULFILLMENT OF THE
REQUIREMENTS FOR THE DEGREE OF

Master of Science
in
Aeronautics and Astronautics
at the
Massachusetts Institute of Technology

February, 1990

©Massachusetts Institute of Technology 1989

Signature of Author _____
Department of Aeronautics and Astronautics
December, 1989

Certified by _____
Professor Edward M. Greitzer
Thesis Supervisor

Accepted by _____
Professor Harold Y. Wachman
Chairman, Departmental Graduate Committee

MASSACHUSETTS INSTITUTE
OF TECHNOLOGY

FEB 26 1990

LIBRARIES

Aero

Abstract

Aerodynamic Design of Moveable Inlet Guide

Vanes for Active Control of Rotating Stall

by

Peter D. Silkowski

Submitted to the department of Aeronautics and Astronautics on

December 18, 1989 in partial fulfillment of the requirements for

the degree of Master of Science in Aeronautics and Astronautics

This thesis describes an analysis of moveable inlet guide vane operation for use in active control of rotating stall in axial flow compressors. The results indicate that blade deflections needed (in degrees) are approximately one half of the sensed axial velocity disturbance (in percent). Models were developed for the blade row, the control perturbations launched by the moving blades, and the compressor. These models were used in a parametric study which showed that from a control wave launching point of view, airfoil camber and mean flow turning of the cascade are unimportant, whereas fraction of blades moved and solidity are the key parameters. Furthermore, the compressor model lead to the result that the more in phase the blade misstaggering is with the velocity disturbance, the more effective the control is. These results were then used to design and build an inlet guide vane row of 12 blades for testing as a stall control device.

Thesis Supervisor: Edward M. Greitzer

Title: Professor of Aeronautics and Astronautics

ACKNOWLEDGEMENTS

The author would like to thank the following:

Professor Greitzer for his guidance and patience.

Professor Epstein and Dr. Guenette for their help with hardware.

Dr. Tan for help in general.

Professor Yamasaki for his help with the unsteady work.

Bob Haimes for his computing knowledge.

All of the students in the GTL, especially my very understanding roomates Earl, Rob, and Bill.

And my parents, Daniel and Loretta Silkowski, and my sister Angelica, for all of their support.

This research was supported by the Air Force Office of Scientific Research under contract AFOSR-87-0398.

Contents

List of Figures

Chapter 1

INTRODUCTION

1.1 Introduction

In many regards, engineering is the science of tradeoffs. For example, in aircraft wing design some aircraft such as the F-14, F-111, and B-1, with their variable sweep wings, are adaptable, and thus are able to fly much closer to the optimal geometric configuration at all phases of the flight envelope, with a trade for increased weight and complexity accompanying the swing wing. Another example of tradeoffs in engineering is that of performance for safety margin, such as the F-16 trading dynamic stability for lower induced drag. This thesis will investigate the possibility of trading performance for complexity, and thus obtaining better performance by operating in a normally unstable region, through adaptable geometry, active control.

1.2 Background

Much as the entire aircraft can have different instabilities, for example dutch roll, phugoid, and short period motion, so can the engine with its instabilities of rotating stall and surge. Whereas surge is considered a system, or "global" instability, rotating stall is a higher frequency "local" instability. Rotating stall consists of a region or regions of blockage rotating around the circumfrence at a fraction of rotor speed. In these regions of blockage, "the blades are severely stalled" and "typically there is negligible net throughflow, with areas of local reverse flow"[1] . These regions of reversed flow can lead to melting of the blades, and the motion of the blades

[1]Reference 2 pg. 135

through the stall cells can cause "large vibratory stresses in the blades" [2]. In rotating stall, "the flow at any local position is quite unsteady; however the annulus averaged mass flow is steady with the stall cells serving only to redistribute this flow" [3]. Although the averages may be steady, they may also be at a much lower value than for the unstalled case, thus representing a loss in engine performance. The most detrimental stall cell configuration is that of a single cell, [1], and as a result, in the models to come, only waves of first harmonic will be considered.

One explanation for the development of rotating stall is given by the simple model in fig.(1.1),[2], where a flow perturbation has caused the angle of incidence of flow on the blade to be too large leading to separation and partial blockage of the blade channel. As a result of this blockage, flow is diverted causing the next blade to stall and the previous blade to unstall or have its angle of incidence decrease. In this way the stall cell propagates around the circumference of the machine. The resulting flow blockage leads to a decrease in stage pressure rise. The original flow perturbation that triggers events, in this model, can either be internal, for example from non-symmetric tip clearance or burner instability or convected into the machine in the form of inlet distortion, caused by poor inlet design, aircraft maneuvers, etc. The goal of an active control scheme is to operate in the linear arena of these small perturbations, catching the problem at its inception, and then controlling it with control perturbations that are small relative to the power levels of the engine. Such strategies have already been demonstrated for surge by Pinsley [18] and Gysling [19].

This thesis investigates the problem of launching these control perturbations and evaluating their effectiveness. In order to accomplish this task a model used by Epstein, Ffowcs Williams, and Greitzer, [4], is extended to include the effects of control wave launching. Methods for predicting the new term that arises in this extension to the model are discussed and then used

[2]Reference 2 pg. 134

[3]Reference 2 pg. 135

to perform a stability analysis. Models of the inlet guide vane row are developed and used to determine how best to physically implement this control. Finally, this information is used in designing and constructing hardware for testing.

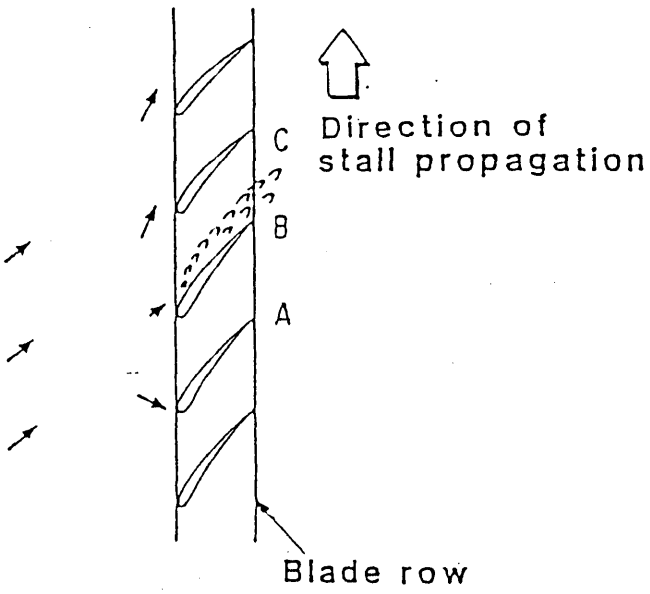

Figure 1.1: Inception of rotating stall [2]

Chapter 2

Modelling the Overall Flowfield and the Compressor

2.1 Compressor Model

Previous analytic models for rotating stall, inlet distortion, and compressor behavior have lead to the general result that growth or decay of disturbances is related to the slope of the compressor characteristic. In particular, decay occurs for $\frac{\partial \Delta P}{\partial C_x} < 0$, growth for $\frac{\partial \Delta P}{\partial C_x} > 0$, with the peak, or zero slope area of the characteristic, $\frac{\partial (P_e - P_{t_{in}})}{\partial C_x} = 0$, often taken as the criterion for the onset of rotating stall and thus the stability boundary. Moveable inlet guide vanes were chosen as the control perturbation launching mechanism in this analysis because of the relatively low technical risk and promise shown in previous work, ([7], [20], [16] and [4]).

The model for the compressor must address the unsteadiness associated with the relative motion of the rotor, stator, and flow disturbance traveling around the annulus. A compressor model which accounts for this effect was used by Epstein, Ffowcs Williams, and Greitzer [4] and will be extended here to include the effect of the control wave launching. The basis of the model is the assumption "that the compressor pressure rise in unsteady flow can be found from the axisymmetric flow performance together with a correction to account for flow unsteadiness"[1]. For example, in the stator

$$\frac{\Delta P}{\rho U^2} = F_s(\phi) - \tau_s \frac{\partial \phi}{\partial t} \tag{2.1}$$

where

[1]Reference 1 pg. 373

$$\tau_s = \frac{b_x}{U cos^2 \gamma} \tag{2.2}$$

$F_s(\phi)$ represents the steady state performance, while τ represents the inertia, and $\frac{\partial \phi}{\partial t}$ the unsteady acceleration of the fluid in the blade row. Similarly, for the rotor

$$\frac{\Delta P}{\rho U^2} = F_r(\phi) - \tau_r(\frac{\partial \phi}{\partial t} + \frac{U}{r}\frac{\partial \phi}{\partial \theta}) \tag{2.3}$$

where the term

$$\tau_r \frac{U}{r}\frac{\partial \phi}{\partial \theta} \tag{2.4}$$

represents the unsteadiness due to the relative motion of the rotor and flow disturbance. An inlet guide vane row is similar to that of the stator except that the pressure rise is written in terms of static to total

$$\frac{P_e - P_{t_{inlet}}}{\rho U^2} = F_{igv}(\phi) - \tau_{igv}\frac{\partial \phi}{\partial t} \tag{2.5}$$

Summing these three contributions to pressure rise, and defining $\lambda = \tau_r \frac{U}{r}$, $\mu = (\tau_r + \tau_s + \tau_{igv})\frac{U}{r}$ and $\Psi_{s.s.}(\phi) = F_{igv}(\phi) + F_r(\phi) + F_s(\phi)$ results in

$$\Psi(\phi) = \frac{P_e - P_{t_{inlet}}}{\rho U^2} = \Psi_{s.s.}(\phi) - \lambda\frac{\partial \phi}{\partial \theta} - \frac{r\mu}{U}\frac{\partial \phi}{\partial t} \tag{2.6}$$

For small amplitude flow perturbations the compressor can be expressed in linearized form as

$$\frac{\delta P_e - \delta P_{t_{in}}}{\rho U^2} = \frac{\partial \Psi_{s.s}}{\partial \phi}\delta\phi - \lambda\frac{\partial \delta\phi}{\partial \theta} - \frac{r\mu}{U}\frac{\partial \delta\phi}{\partial t} = \delta\Psi(\phi) \tag{2.7}$$

In this investigation of control perturbations caused by moveable inlet guide vanes, the compressor model must be expanded to include these perturbations. For a compressor with moveable inlet guide vanes, the steady state pressure rise through the machine is not only a function of ϕ, but also a function of flow angles, and therefore γ, inlet guide vane stagger angle. For example, in steady flow with flat plate airfoils assuming no separation, and high solidity, such that flow angle equals blade stagger angle around the entire circumference of the machine,

the Euler Turbine equation gives pressure rise as a function of γ and ϕ as opposed to a function of ϕ only.

$$\frac{\Delta P_t}{\rho} = U^2[1 - \phi(tanB_c^{'} + tan\gamma)] \tag{2.8}$$

Similarly then, $\Psi_{s.s.}(\phi)$ is really $\Psi_{s.s}(\phi, \gamma)$ and hence $\delta\Psi_{s.s}$ is given by $\delta\Psi_{s.s.} = \frac{\partial\Psi}{\partial\phi}\delta\phi + \frac{\partial\Psi}{\partial\gamma}\delta\gamma$. Equations (2.6) and (2.7) become

$$\Psi(\phi) = \Psi_{s.s.}(\phi, \gamma) - \lambda\frac{\partial\phi}{\partial\theta} - \frac{r\mu}{U}\frac{\partial\phi}{\partial t} \tag{2.9}$$

$$\delta\Psi(\phi) = \frac{\partial\Psi_{s.s.}}{\partial\phi}\delta\phi + \frac{\partial\Psi_{s.s.}}{\partial\gamma}\delta\gamma - \lambda\frac{\partial\delta\phi}{\partial\theta} - \frac{r\mu}{U}\frac{\partial\delta\phi}{\partial t} \tag{2.10}$$

the resulting model for the compressor.

2.2 Modelling the Upstream and Downstream Flowfields

In addition to the pressure rise model developed for the compressor, it is assumed that the machine is of high hub to tip ratio so that the problem becomes 2-D in θ,z space. In this 2-D space, the compressor is "unwraped" as a cascade from 0 to 2π, or similarily, as an infinite cascade arrangement with period 2π. Furthermore, the compressor is considered to operate in a constant area duct far enough away from any other components of the engine, to prevent coupling. Addressing the upstream flowfield first, far upstream, the flow is steady, and parallel. There is nothing to cause streamline curvature, hence static pressure is constant with θ. In addition, the flow upstream is irrotational, and assuming inviscid flow, it remains irrotational up to the compressor face from Kelvin's thereom.

In the neighborhood of the compressor, there is a possibility for unsteady effects as a result of the relative motion of the rotors and stators. However, upon a closer inspection of the rotor, modeled as a row of moving vortices, representing the bound vorticity of the loaded rotor airfoils, it can be seen that the effects on v, P_t, and P die off as $e^{\frac{x}{r}}$, away from the compressor in both the upstream and downstream directions. The compressor then is not a passive player in the

system, but instead does send out small disturbances of its own, $u', v' \sim e^{nx/r}$, to redistribute the flowfield entering the machine [2].

It is convenient to cast the problem in terms of a perturbation stream function, ψ_u. Continuity is then automatically satisfied, and irrotationality becomes Laplace's equation $\nabla^2 \psi_u = 0$. Solving this equation, subject to the exponential boundedness condition discussed above, results in

$$\psi_u = A_n e^{in(\theta - \sigma t) + nx/r} \tag{2.11}$$

The upstream flow field is then represented as $U = \bar{U} + u'$, $V = v'$, $P = \bar{P} + p'$ and

$$u' = \frac{1}{r}\frac{\partial \psi}{\partial \theta} = \frac{in}{r} A_n e^{in(\theta - \sigma t) + nx/r} \tag{2.12}$$

$$v' = -\frac{\partial \psi}{\partial x} = -\frac{n}{r} A_n e^{in(\theta - \sigma t) + nx/r} \tag{2.13}$$

Writing Euler's equation in terms of these mean and perturbation quantities

$$-\frac{\partial P}{\partial x} = \rho[\frac{\partial}{\partial t}(\bar{U} + u') + (\bar{U} + u')\frac{\partial}{\partial x}(\bar{U} + u') + \frac{v'}{r}\frac{\partial}{\partial \theta}(\bar{U} + u')] \tag{2.14}$$

then expanding, keeping only first order terms, subtracting the mean flow equation, and noting that $\frac{\partial \bar{U}}{\partial \theta} = 0$ and therefore $\frac{\partial \bar{U}}{\partial x} = 0$ from continuity, results in

$$-\frac{\partial p'}{\partial x} = \rho[\frac{\partial u'}{\partial t} + \bar{U}\frac{\partial u'}{\partial x}] \tag{2.15}$$

which can be written in terms of total pressure

$$\frac{\partial p_t'}{\partial x} = -\rho\frac{\partial u'}{\partial t} = \frac{\partial}{\partial x}(p' + \rho \bar{U} u') \tag{2.16}$$

Finally, $\nabla^2 p_t' = 0$ from the divergence of Crocco's equation, and therefore, p_t' is of the form $B_n e^{in(\theta - \sigma t) + nx/r}$.

Downstream, the flow is isentropic and inviscid. However, after passing through the compressor, the flow now has a rotational and an irrotational part. The irrotational portion of the downstream flowfield is solved in the same manner as for the upstream, resulting in

$\psi_{Ird} = I_n e^{in(\theta-\sigma t)-nx/r}$. The rotational part is solved for as follows. Using Kelvin's Thereom again, for 2-D inviscid flow gives $\frac{D\omega}{Dt} = 0$, which after expansion and linearization gives

$$\frac{\partial \omega'}{\partial t} + \bar{U}\frac{\partial \omega'}{\partial x} = 0 \tag{2.17}$$

with solution $\omega' \sim e^{in(\theta-\sigma t+\frac{\sigma x}{\bar{U}})}$. This vorticity is then used in Poisson's equation, $\nabla^2\psi_d = -\omega'$, which has solution

$$\psi_d = I_n e^{in(\theta-\sigma t)-nx/r} + R_n e^{in(\theta-\sigma t+\frac{\sigma x}{\bar{U}})} \tag{2.18}$$

$$u_d' = \frac{in}{r}[I_n e^{in(\theta-\sigma t)-nx/r} + R_n e^{in(\theta-\sigma t+\frac{\sigma x}{\bar{U}})}] \tag{2.19}$$

$$v_d' = \frac{n}{r} I_n e^{in(\theta-\sigma t)-nx/r} - \frac{in\sigma}{\bar{U}} R_n e^{in(\theta-\sigma t+\frac{\sigma x}{\bar{U}})} \tag{2.20}$$

By combining the linearized 2-D equations of motion it can be seen that the pressure perturbation must satisfy Laplace's equation, $\nabla^2 p' = 0$ with solution $p' = C_n e^{in(\theta-\sigma t)-nx/r}$, [6]. As with the upstream flow, far enough downstream, the static pressure is again constant with θ. Finally, assuming constant leaving angle at the exit implies $\frac{\partial u'}{\partial x} = 0|_{at\ compressor\ exit}$ from continuity, and then equation (2.15) gives $\frac{\partial p'}{\partial x} = -\rho\frac{\partial u'}{\partial t}|_{at\ compressor\ exit}$.

The upstream, and downstream flowfields are matched across the compressor. The compressor is assumed to have close axial spacing, so that there is no crossflow in the θ direction, and $u = u_u = u_d$. Substituting in for the various terms in the compressor equation

$$\delta\Psi(\phi) = \frac{\partial \Psi_{s.s.}}{\partial \phi}\delta\phi + \frac{\partial \Psi_{s.s.}}{\partial \gamma}\delta\gamma - \lambda\frac{\partial \delta\phi}{\partial \theta} - \frac{r\mu}{U}\frac{\partial \delta\phi}{\partial t} \tag{2.21}$$

where $\delta\phi = \frac{u'}{U}$, and $\delta\gamma = 0$ for the control off baseline case, results in

$$-\frac{2ri\sigma}{U} = \frac{\partial \psi}{\partial \phi} - \lambda in + \frac{r\mu}{U} in\sigma \tag{2.22}$$

$$\sigma = \sigma_r + i\sigma_i$$

Defining the stability boundary at σ_i=0, zero temporal growth rate, the two resulting equations are

$$real \Rightarrow 0 = \frac{\partial \psi}{\partial \phi} \tag{2.23}$$

$$imaginary \Rightarrow \sigma_r = \frac{U\lambda n}{2r + r\mu n} \tag{2.24}$$

As stated earlier, the stability boarder is at the peak of the characteristic.

With control, solving the system of equations in the same manner, gives

$$-\frac{2ri\sigma}{U}\delta\phi = \frac{\partial\psi}{\partial\phi}\delta\phi + \frac{\partial\psi}{\partial\gamma}\delta\gamma - \lambda in\delta\phi + \frac{r\mu}{U}in\sigma\delta\phi \tag{2.25}$$

Assuming a linear control scheme of $\delta\gamma = z\delta\phi$ results in

$$-\frac{2ri\sigma}{U} = \frac{\partial\psi}{\partial\phi} + \frac{\partial\psi}{\partial\gamma}z - \lambda in + \frac{r\mu}{U}in\sigma \tag{2.26}$$

Again, solving for the stability boundary, with $\sigma = \sigma_r$ and $z = z_r + iz_i$

$$real \Rightarrow \frac{\partial\psi}{\partial\phi} + \frac{\partial\psi}{\partial\gamma}z_r = 0 \tag{2.27}$$

$$imaginary \Rightarrow \sigma_r = \frac{U(\lambda n - \frac{\partial\psi}{\partial\gamma}z_i)}{2r + r\mu n} \tag{2.28}$$

If $\psi(\phi)$, $\frac{\partial\psi}{\partial\gamma}(\phi)$ and $\frac{\partial\psi}{\partial\phi}(\phi)$ are all known, then these two equations can be solved to find the stability boundary, and stall cell propagation speed.

2.3 Evaluation of $\psi(\phi)$, $\frac{\partial\psi}{\partial\gamma}(\phi)$ and $\frac{\partial\psi}{\partial\phi}(\phi)$

These three terms are required to solve the stability boundary equation. Starting with $\frac{\partial\psi}{\partial\gamma}(\phi)$, a first guess at this value could be estimated by taking the derivative of the equation (2.8) which results in $\frac{\partial\psi}{\partial\gamma}$ =-$\phi sec^2\gamma$. However, a more accurate method would be to look at different compressor characteristics, for different stagger profiles and at a given ϕ calculate $\frac{\partial\psi}{\partial\gamma}$ from the discrete defenition of derivative

$$\frac{\partial\psi}{\partial\gamma} \sim \frac{\psi_2 - \psi_1}{\gamma_2 - \gamma_1} \tag{2.29}$$

fig.(2.1).

To carry out such work, a code written by Chen based on [12] to calculate compressor performance was modified, and used, resulting in $\psi(\phi)$, fig.(2.1,2.2). The code does not agree well with data, and in particular, the characteristic does not peak over, as in the actual case. In other words, the loses at low ϕ associated with the separation and stalling of the blades, are not well accounted for. However, this peak of the characteristic, and lower values of ϕ are precisely the areas of interest here. Because of the inaccuracy in this region, the differencing procedure was carried out experimentally, with measurements taken on the MIT single stage compressor at three different inlet guide vane stagger settings by Schulmeyer, the baseline, fig(2.2), and inlet guide vane restaggerings of $\pm 7.5°$ fig (2.3). Here, the characteristics peak over as expected, but there are not many points to the left of the peak, and the characteristics all start to coalesce at the peak, causing $\frac{\partial \psi}{\partial \gamma}$ to approach 0. To fill in this missing information, parabolas were fit to the characteristics, by fitting a quadratic through two points of the characteristic, and matching slopes at the peak, fig.(2.4). The two common points were chosen near the peak again since this is the region of interest. Using these three curve fits for $\psi(\phi)$, $\frac{\partial \psi}{\partial \gamma}(\phi)$ can be found for the baseline, fig.(2.5), $\gamma_{igv} = 15°$, case from the definition of discrete derivative mentioned above, and $\frac{\partial \psi}{\partial \phi}(\phi)$ from direct differentiation. Substituting, in the stability boundary equation (2.27), results in an equation for $\phi_{stability\ boundary}$ with z as a parameter. Solutions for several values of z are plotted in fig(2.6,2.7). From this plot, it is seen that control is effective, $\phi_{s.b.-control\ on} < \phi_{s.b.-control\ off}$ whenever $z_r > 0$, in other words, the more in phase $\delta\gamma$ and $\delta\phi$ are, the more effective is the control for a given magnitude of z.

2.4 Determining the Required Inlet Guide Vane Stagger Profile

Let the flow disturbance, $\delta\phi$, and blade mistagger profile, $\delta\gamma$, be represented by Fourier series, $\delta\phi = \sum \delta\phi_n e^{in(\theta-\sigma t)}$, $\delta\gamma = \sum G_n e^{in(\theta-\sigma t)}$. To estimate γ as a function of θ it was assumed that each blade controlls the zone of its maximum projection onto the r,θ plane, ie. half chord below the blade to half chord above it in the form of a step function, and stagger is defined over the entire 1 chord area, and equal to its value on the blade. Between these zones stagger is defined as 0.

Then from the control law $\delta\gamma = z\delta\phi$, $G_n = z\delta\phi_n$ for all of the harmonics, and one can determine the mistagger profile, $\delta\gamma$, required for control of a given perturbation, $\delta\phi$, with parameter z. Recalling that only waves of first harmonic will be looked at, the question arises as to what $d\gamma$ profile will give the first Fourier coefficient. Basically, this is a problem in representing a continuous wave in discrete fashion, and an important parameter will be the degree of discreteness, or discrete/continuous ratio which is best represented by the solidity, and fraction of blades moved. The limiting case as solidity approaches infinity, and all blades are moveable will be referred to as the continuous case.

For analysis, will consider a cosine, one harmonic, $\delta\phi$ perturbation. Then $\delta\phi = |\delta\phi| cos(\theta) = |\delta\phi| \sum \delta\phi_n e^{in(\theta-\sigma t)}$, with $\delta\phi_1$ known from Fourier decomposition of the unit cosine wave. In the limiting continuous case, the maximum mistaggering required, $DG_{cont.}$, is $z|\delta\phi|$ and from $\delta\gamma = z\delta\phi$, $G_1 = z|\delta\phi|\delta\phi_1$ fig.(2.8). On the otherhand, when a discrete case like fig.(2.9) is Fourier transformed it has a first Fourier coefficient, $G_{1_{disc.}}$, that is not necessarily the same as the required $G_{1_{cont.}}$. However, since Fourier series representation is linear, the required $G_{1_{cont.}}$ can be achieved using this discrete representation, if the spikes are altered by the factor $\frac{G_{1cont.}}{G_{1_{disc.}}}$. Multiplying by this factor results in fig. (2.10), which shows that the maximum amount of blade

deflection for this particular discrete case is roughly six times that needed in the continuous case , $\frac{DG_{disc}}{DG_{cont.}}$ ~6. Similar calculations were performed for fig.(2.11,2.12) which when Fourier decomposed, all have $G_1 = z|\delta\phi|\delta\phi_1$. For a fixed number of blades, the spacing is also fixed and therfore solidity and chord are proportional. As solidity changes, the size of the zone influenced by each blade will also change proportionally. This explains why the spike widths in fig(2.10,2.11,2.12) differ by a factor of 2.

This factor, $\frac{G_{1cont.}}{G_{1_{disc.}}}$, is a complex number, Fe^{iP}, and therefore can involve a change in both magnitude and phase of the original dγ profile. However since the location of the blades is fixed, this phase shift of the function cannot be accomplished by translating the plot $\pm$P degrees, fig(2.13). Instead, both changes are accomplished by altering spike heights only, fig(2.14), and no shifting of spike locations is required. This is demonstrated for F=2, P=$\frac{\pi}{8}$ in fig(2.13,2.14). Therefore, for any discrete configuration and required $G_{1_{cont.}}$, the ratio $\frac{DG_{disc}}{DG_{cont.}} = |\frac{G_{1_{cont.}}}{G_{1_{disc.}}}|$ =(max. mistagger disc.)/(max. mistagger cont.) will create the correct $d\gamma(\theta)$ profile to acheive the required $G_{1_{cont}}$.

Two cases were examined. In the first case the moveable blades were either in an "on" or "off" position , and in the second case, the magnitude of blade mistagger was variable. Runs were done for 48 blades at a solidity of .5 and 1. Some results of this analysis are seen in fig.(2.10,2.11,2.12) displaying the various $\delta\gamma$ profiles required for control. Figure(2.15) is a summary of these calculations, which basically confirms that for a given desired wave form $G_{1_{cont.}}$, the maximum amplitude of discrete turning, DG_{disc}, decreases as the fraction of blades moved increases, or as solidity increases. The two and four blade cases have the same value because the four blade case degenerates to the two blade case, since for the cosine distribution, two of the blades are at $\pi/2$ and $3\pi/2$ and hence their misstagger, $d\gamma$=0. These relations hold independent of the value of the common factor $z|\delta\phi|$.

For example, consider the case of $z = Re^{iB} = 1$ and $\delta\phi = 1\%$ of mean flow. From fig.(2.6,2.7)

$\frac{\Delta\phi_{s.b.}}{\phi_{s.b.-control\ off}}$ =-.056 and from fig.(2.4) $\phi_{s.b.-control\ off}$=.4, so $\bar{\phi}$ = .38, and $\delta\phi$=.0038. If only half of the blades are moveable, fig.(2.15) gives the factor $\frac{DG_{disc}}{DG_{cont.}}$=1.98. It has been shown that DG, the maximum required discrete mistaggering, is the product of this factor and the continuous value, $z|\delta\phi|$, resulting in DG=.43 degrees. Therefore, to keep the compressor stable to a 1% $\delta\phi$ perturbation at a $\bar{\phi}$ of .38, requires a maximum blade deflection of roughly half a degree, which is allowable.

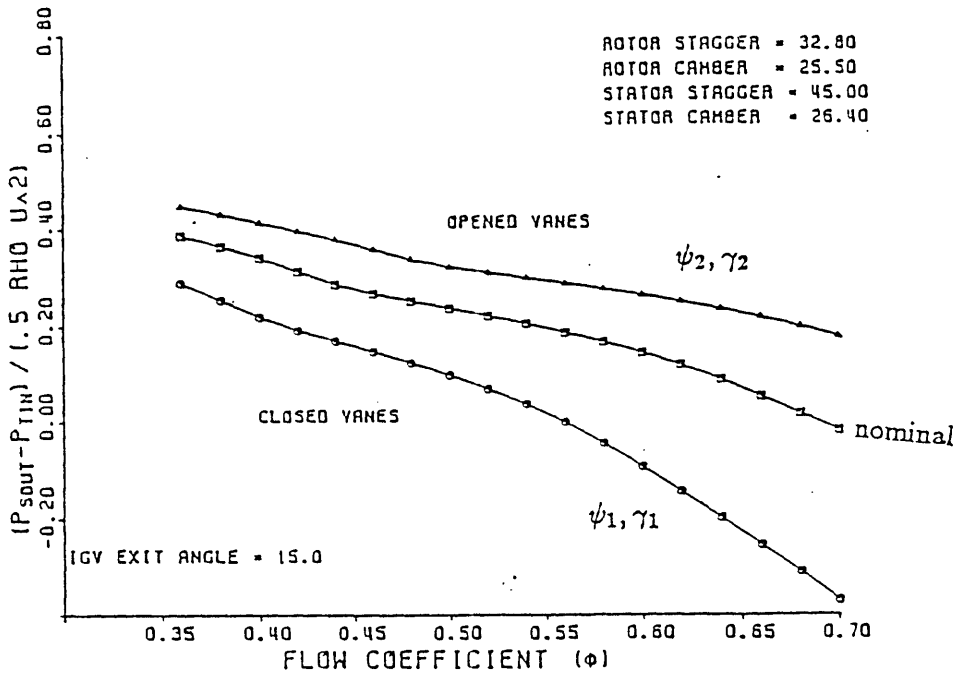

Figure 2.1: Calculated compressor speedlines with a 10 degree opening and closing of igv's

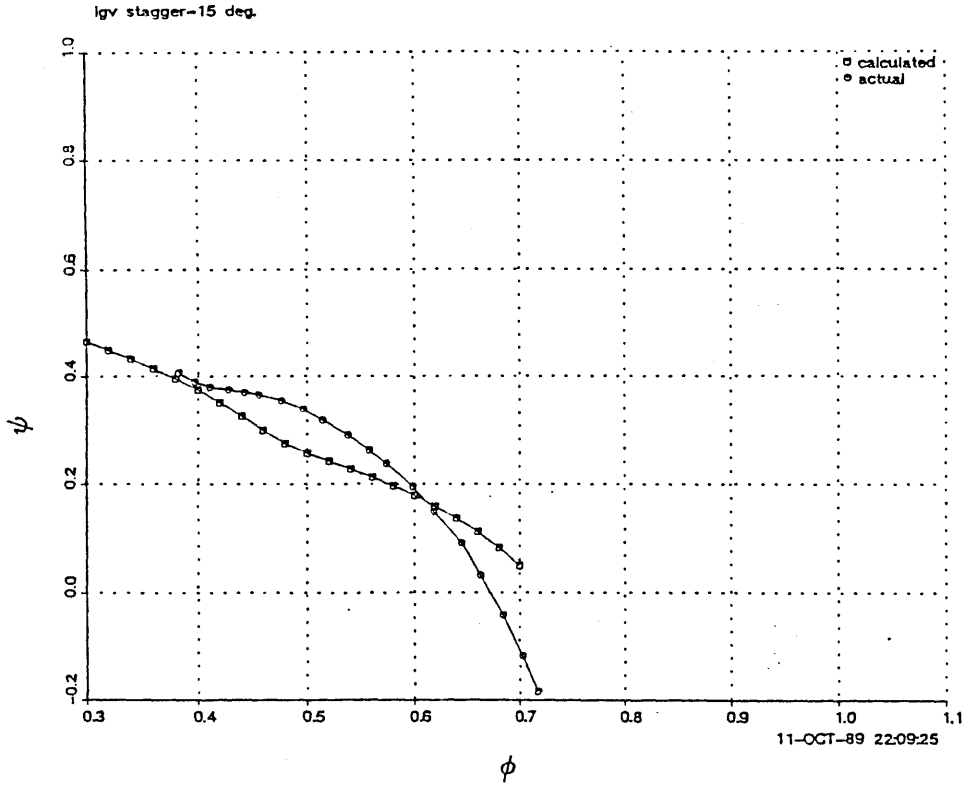

Figure 2.2: Baseline compressor, calculated and actual, speedlines [20]

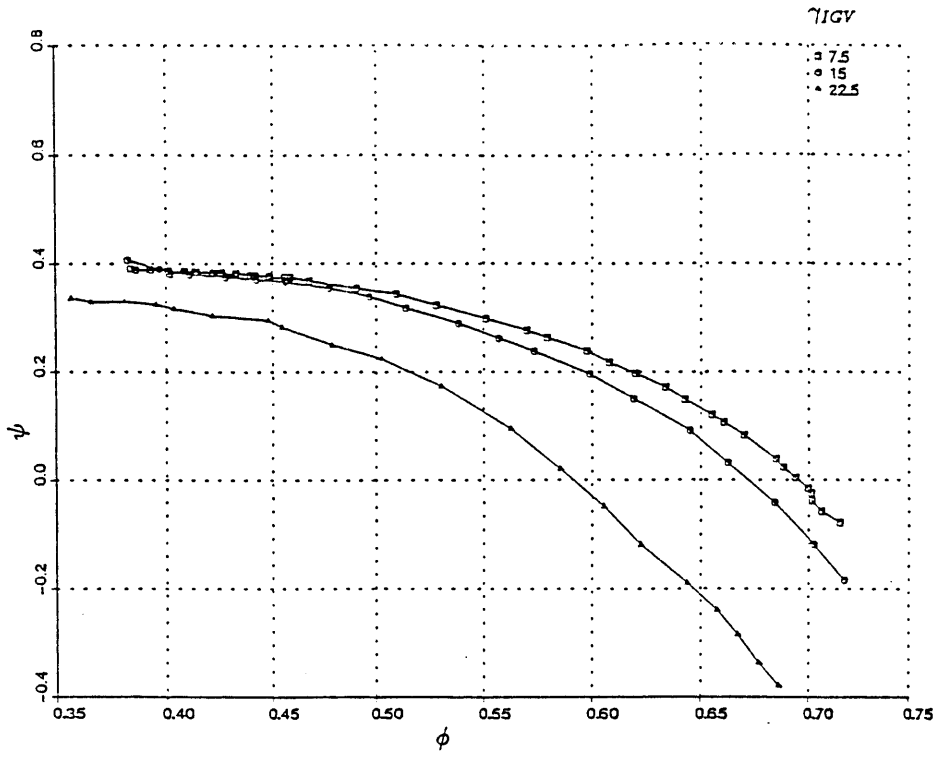

Figure 2.3: Speedlines of restaggered machine

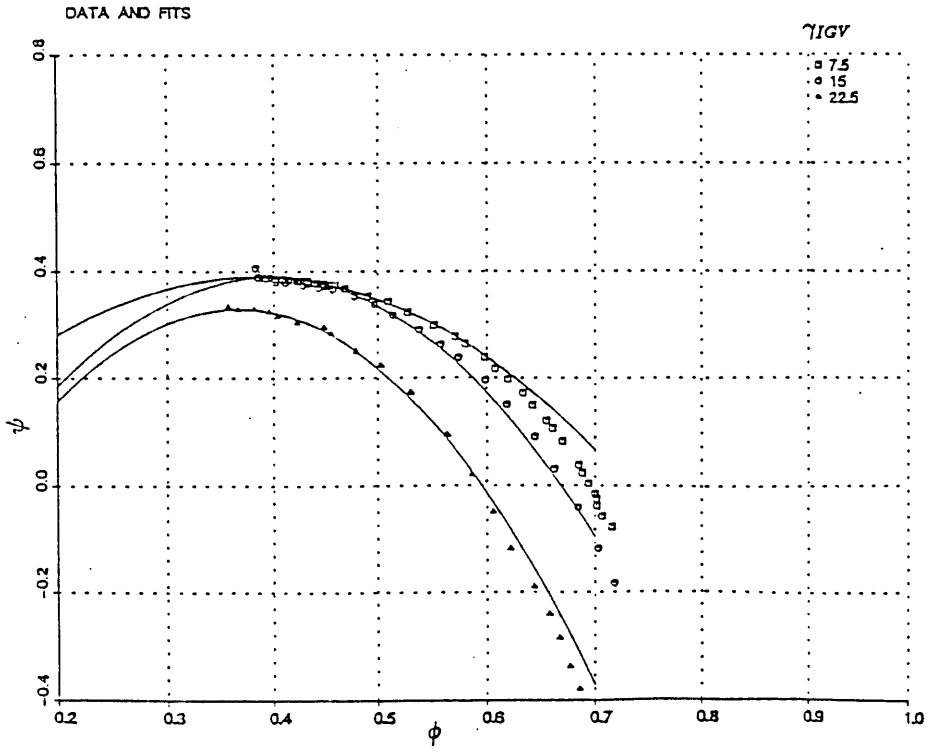

Figure 2.4: Parabolic fits

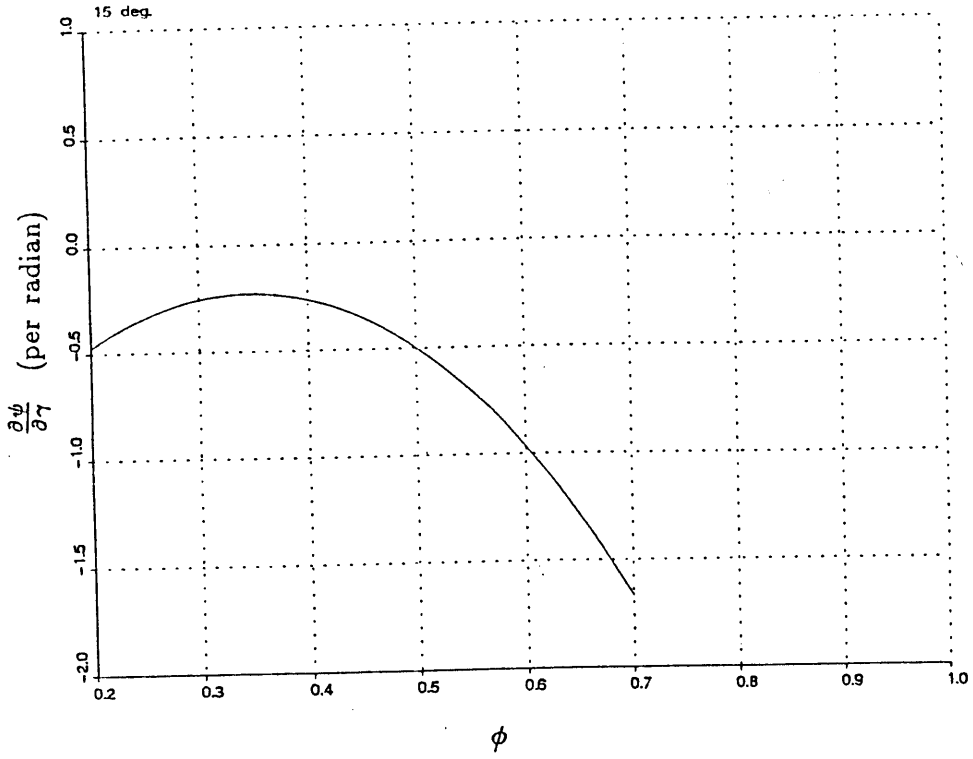

Figure 2.5: $\frac{\partial\psi}{\partial\gamma}$ for γ_{igv}=15

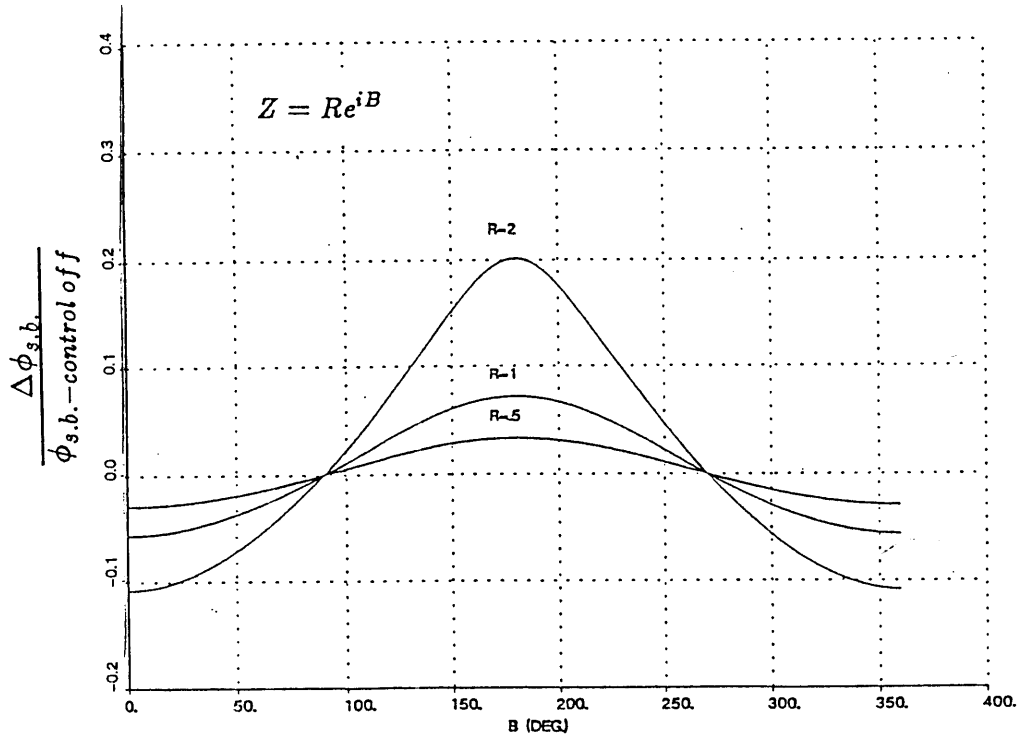

Figure 2.6: Percent change in stability boundary, with R as a parameter and $\gamma_{igv} = 15$

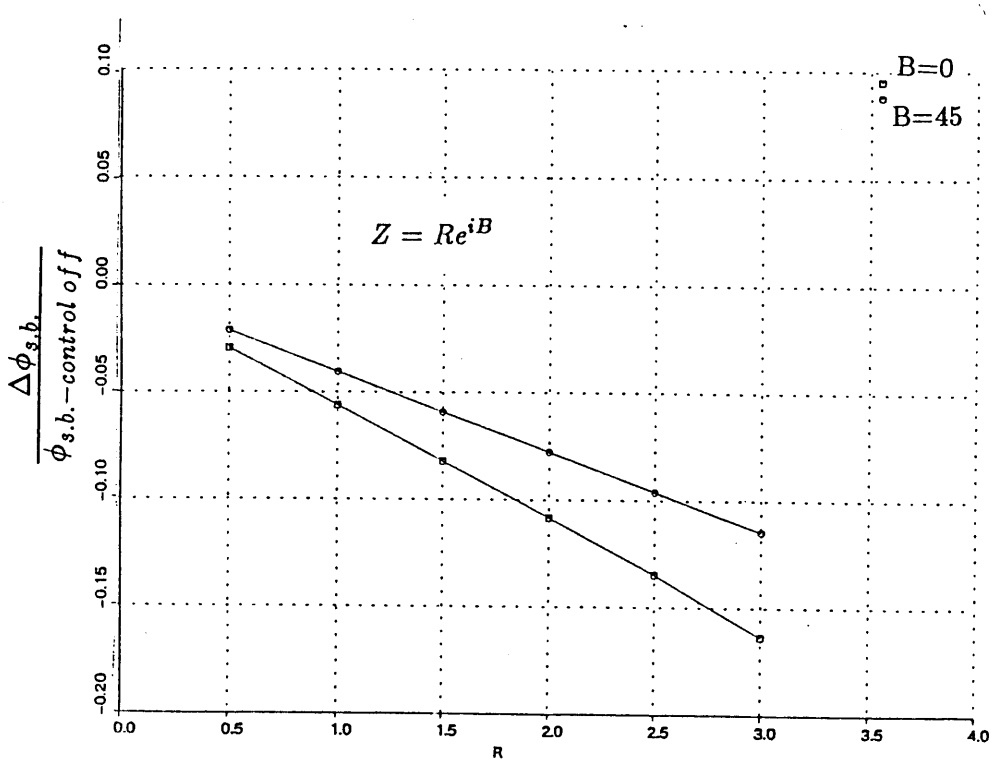

Figure 2.7: Percent change in stability boundary, with B as parameter and $\gamma_{igv} = 15$

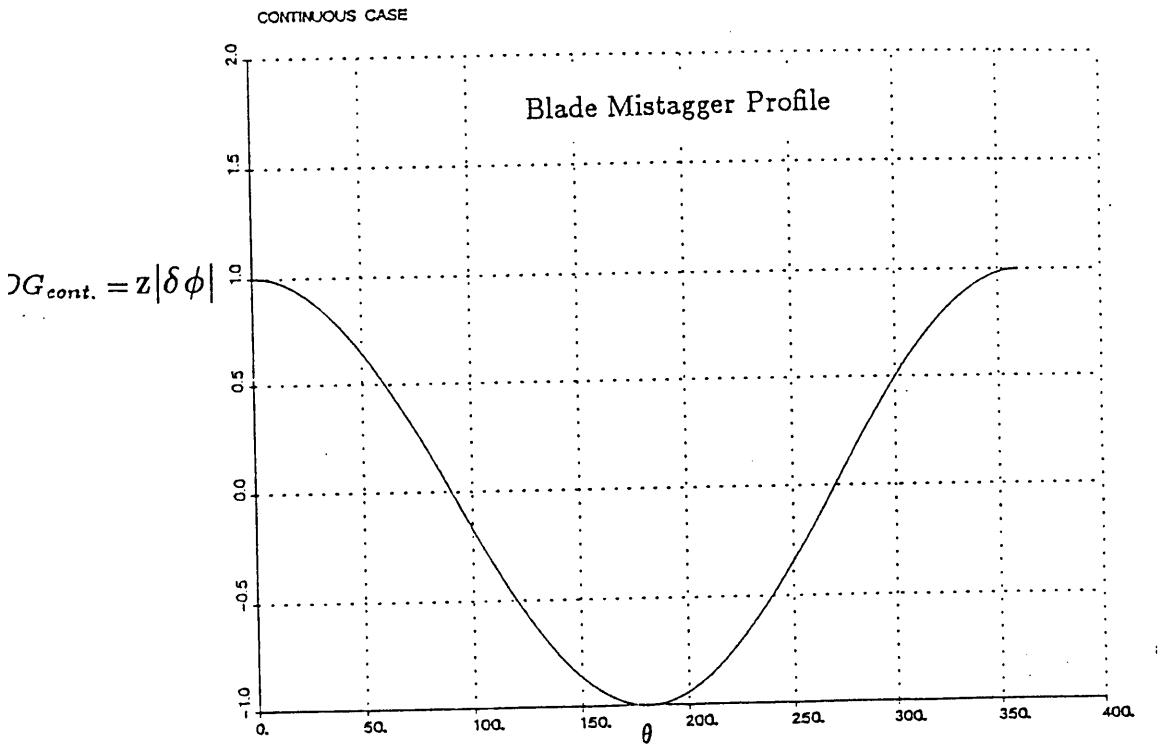

Figure 2.8: Continuous case

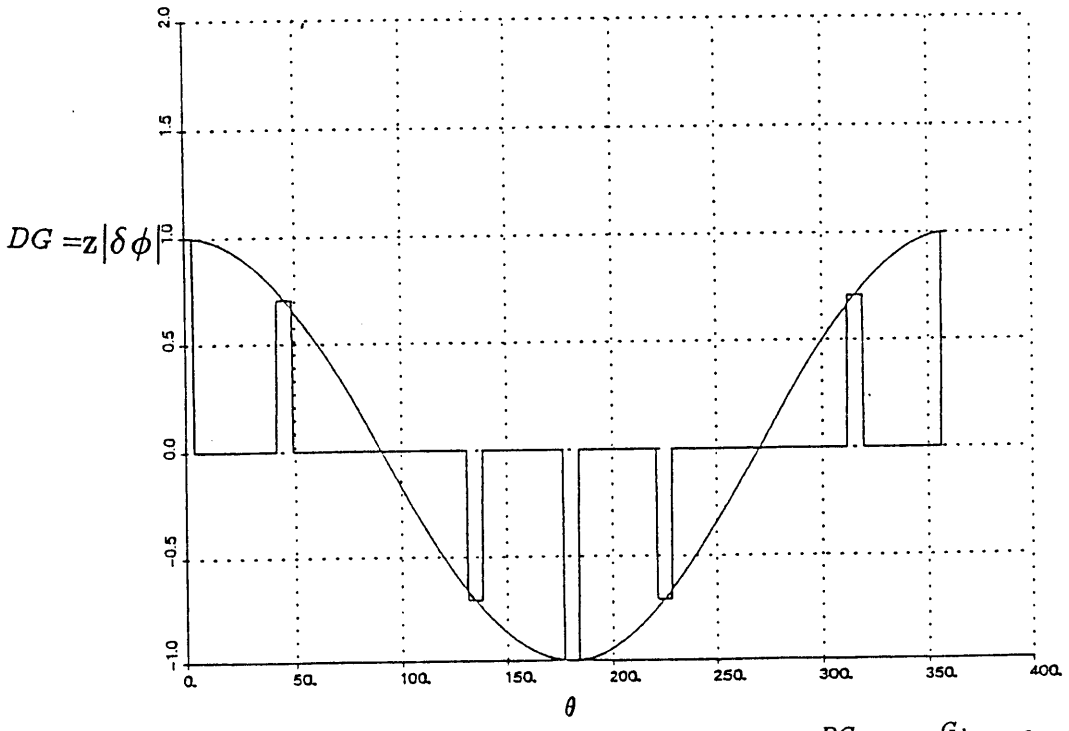

Figure 2.9: Misstagger profile before multiplication by factor, $\frac{DG_{disc}}{DG_{cont}} = \frac{G1_{cont}}{G1_{disc}}$ for 8 moveable blades out of 48 total, with $\sigma = 1.0$. DG=maximum amount of blade mistagger.

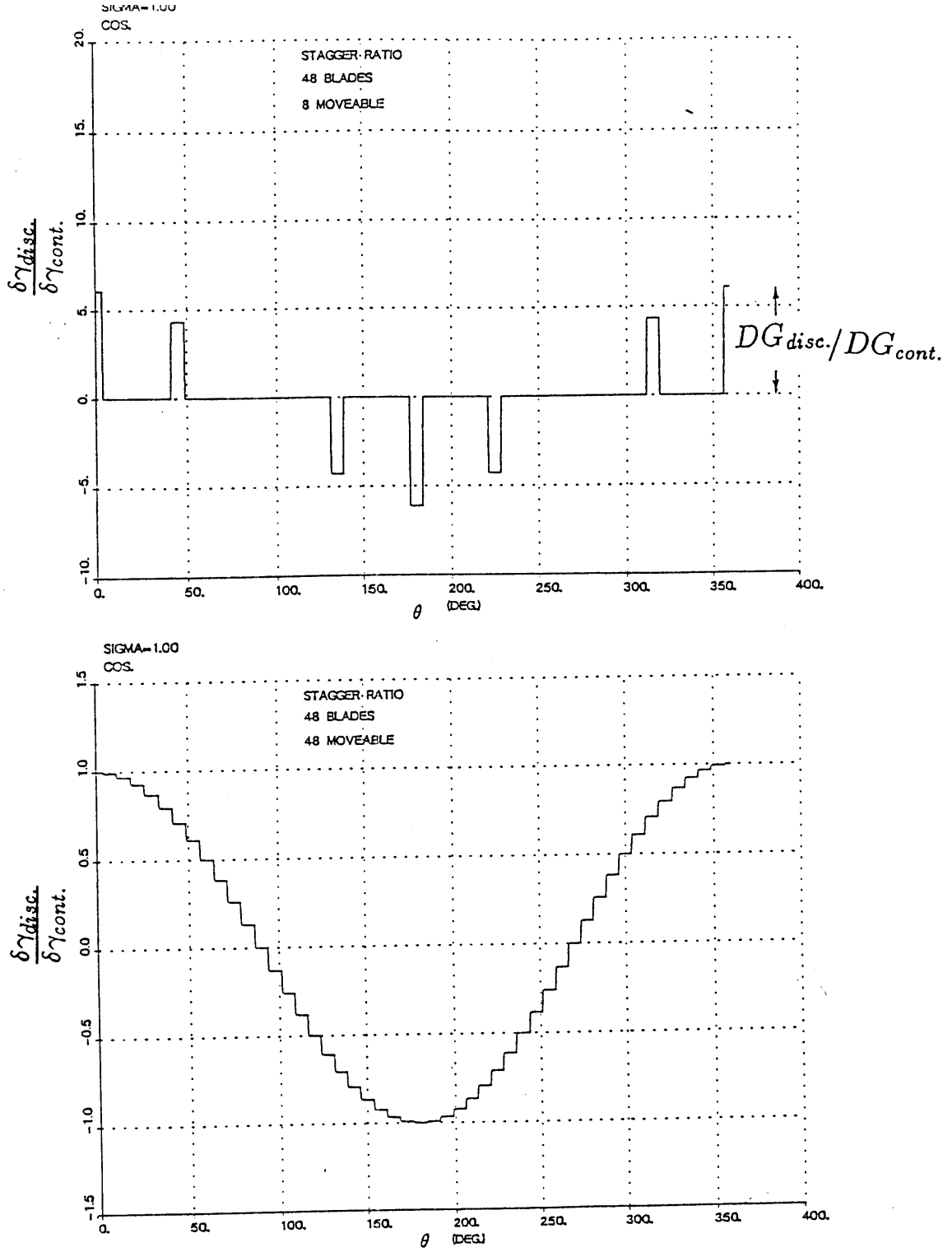

Figure 2.10: Stagger ratio profile with first Fourier coefficient G_1=z$|\delta\phi|\delta\phi_1$. DG=maximum amount of mistagger

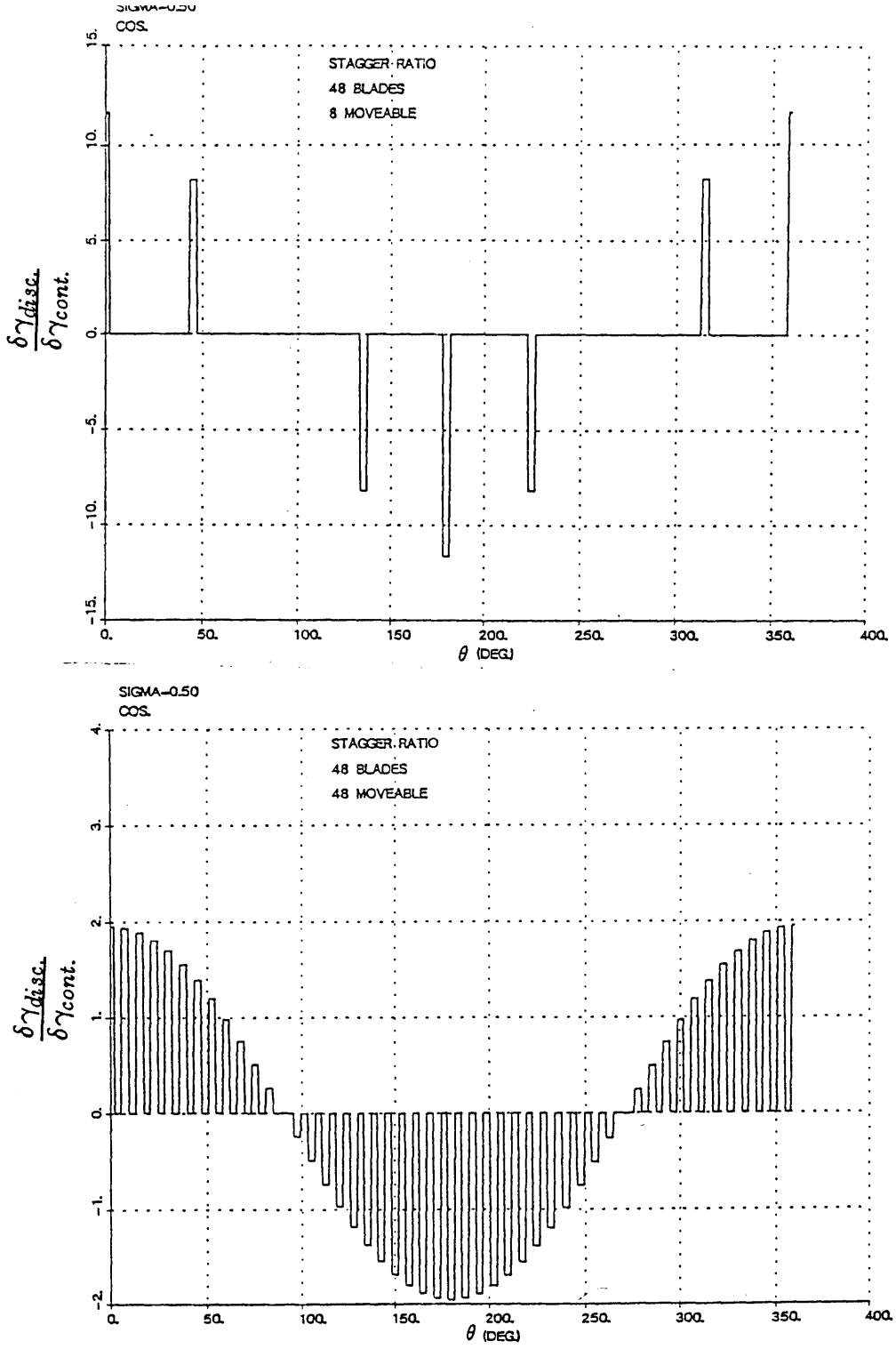

Figure 2.11: Stagger ratio profile with first Fourier coefficient G_1=z$|\delta\phi|\delta\phi_1$. Note $\sigma = .5$ and therefore the spike widths are half of the previous figure's

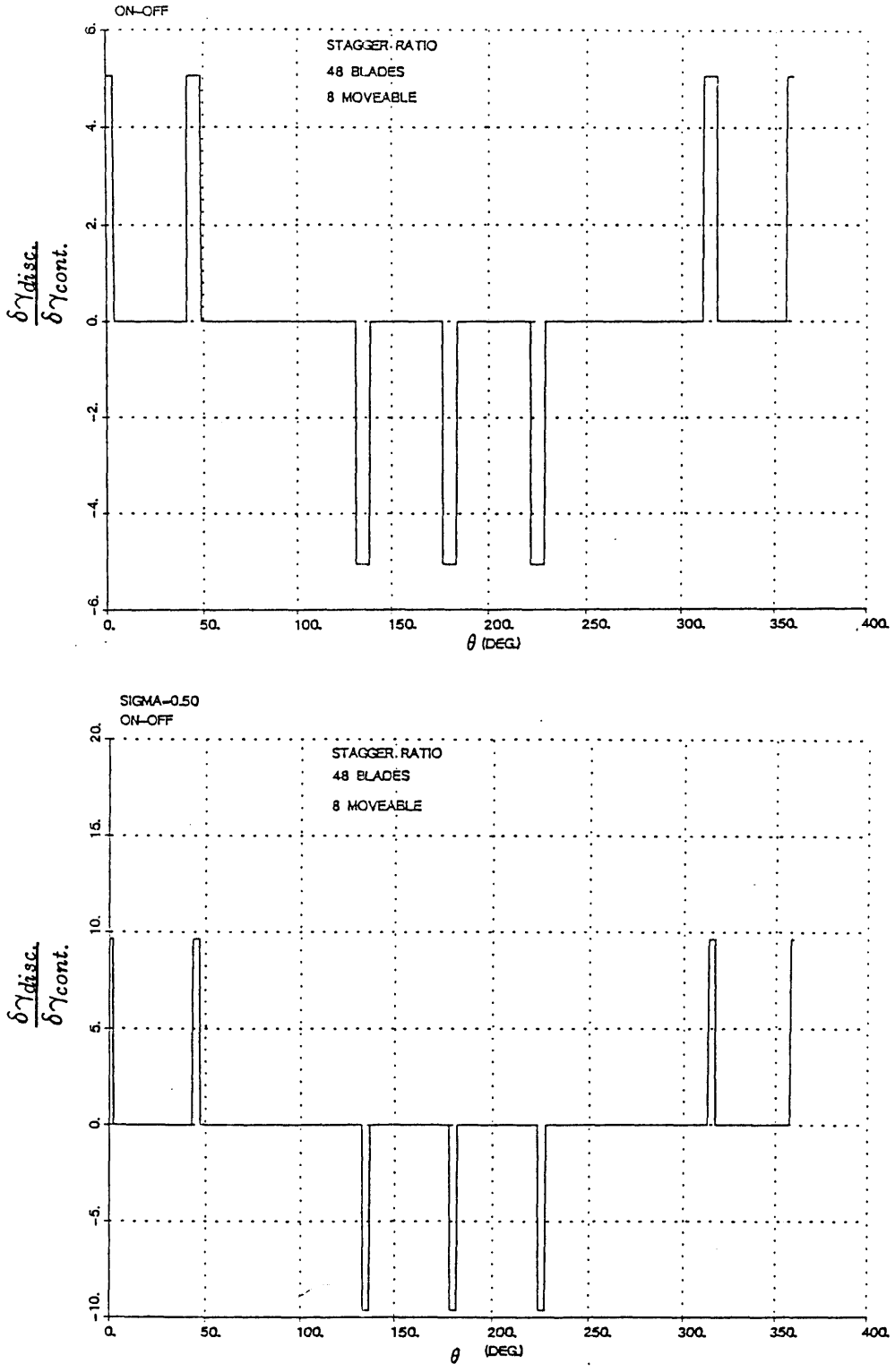

Figure 2.12: Stagger ratio profile with first Fourier coefficient G_1=z$|\delta\phi|\delta\phi_1$., on-off scheme

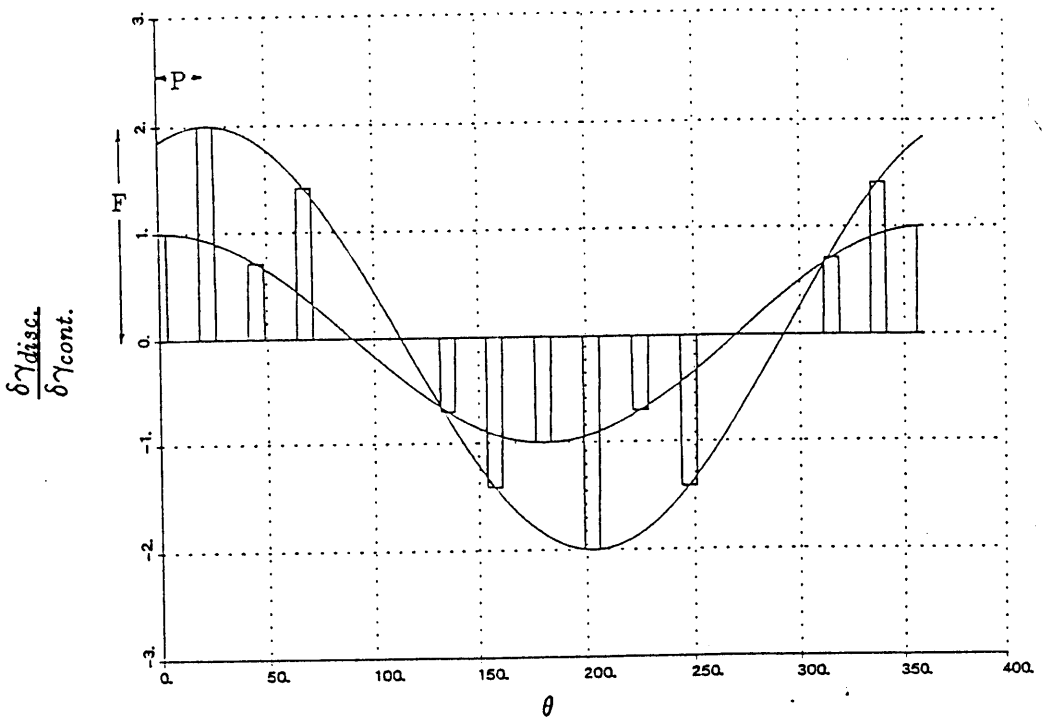

Figure 2.13: Changing both magnitude and phase of enveloping, discretized, function by changing both spike heights and spike locations for F=2, P=$\frac{\pi}{8}$

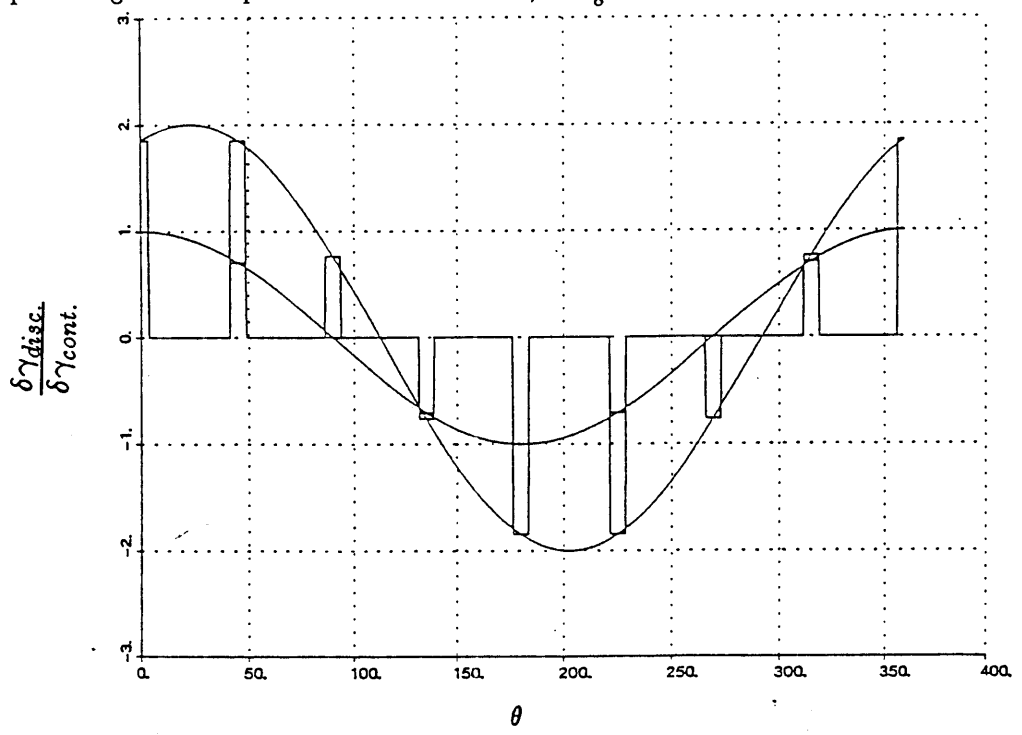

Figure 2.14: Changing both magnitude and phase of enveloping, discretized, function by changing spike heights only, and not spike locations for F=2, P=$\frac{\pi}{8}$

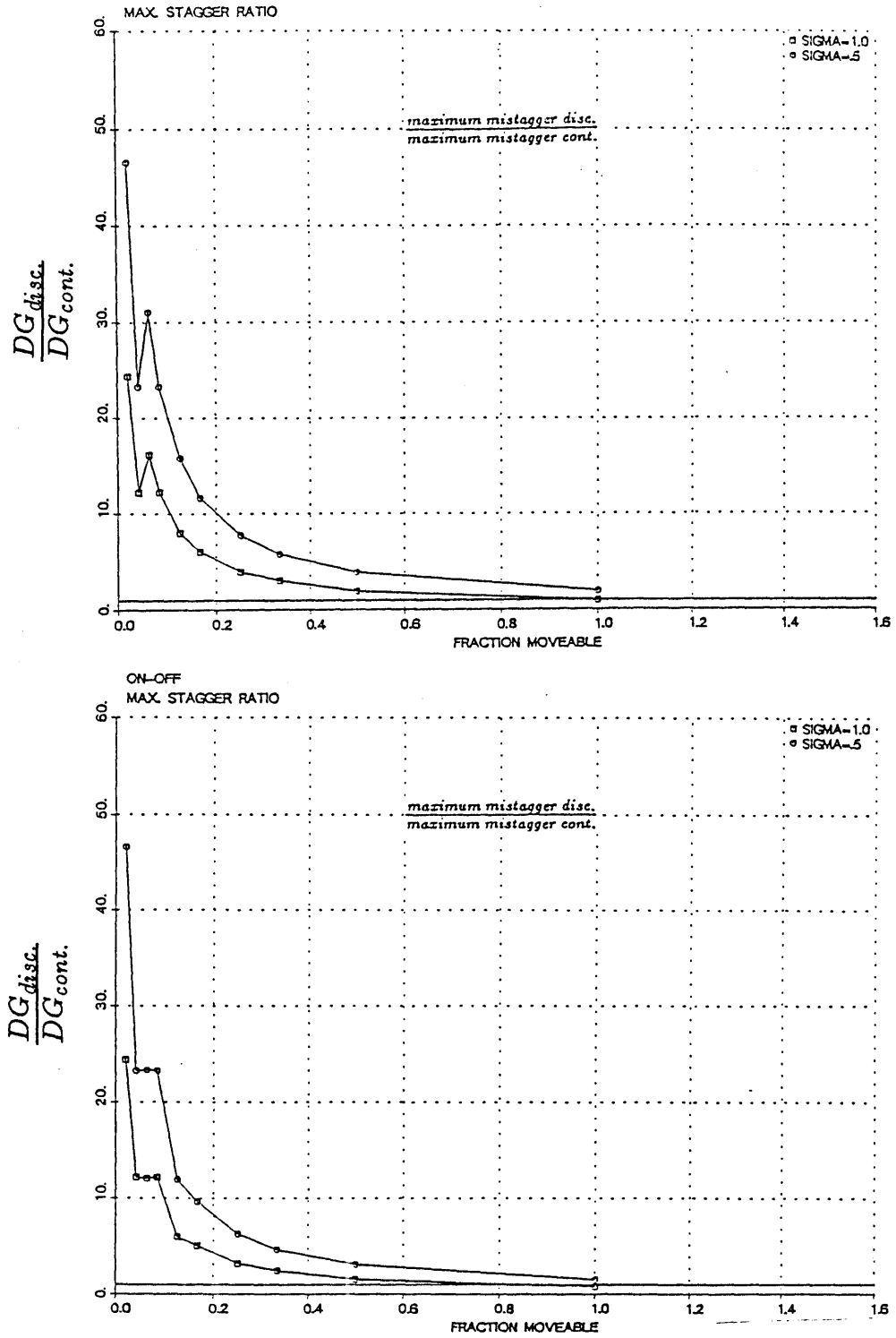

Figure 2.15: Maximum mistaggering ratio required to achieve a given $G_1 = z|\delta\phi|\delta\phi_1$. 48 total blades. Asymptotes to 1

Chapter 3

Steady potential calculation of $\frac{\partial \alpha}{\partial \gamma}$

3.1 The New Term, $\frac{\partial \alpha}{\partial \gamma}$

In the previous analysis, the perturbation pressure rise was represented by the term $\delta\psi = \frac{\partial \psi}{\partial \gamma}\delta\gamma$, with γ treated as a step function. As mentioned earlier, the pressure rise through the machine actually depends on flow angle, and stagger angle implicitly since flow angle is a function of blade stagger, $\psi = \psi(\phi, \alpha(\gamma))$. Modelling this effect through the compressor will then alter the term $\frac{\partial \psi}{\partial \gamma}\delta\gamma$ of the compressor equation (2.10) to $\frac{\partial \psi}{\partial \alpha}\delta\alpha = \frac{\partial \psi}{\partial \alpha}\frac{\partial \alpha}{\partial \gamma}\delta\gamma$. The term, $\frac{\partial \alpha}{\partial \gamma}$, represents the relationship between blade stagger and flow angle. Making this change in the compressor equation leads to

$$\delta\Psi(\phi) = \frac{\partial \Psi_{s.s.}}{\partial \phi}\delta\phi + \frac{\partial \Psi_{s.s.}}{\partial \alpha}\frac{\partial \alpha}{\partial \gamma}\delta\gamma - \lambda\frac{\partial \delta\phi}{\partial \theta} - \frac{r\mu}{U}\frac{\partial \delta\phi}{\partial t} \tag{3.1}$$

Letting $\delta\alpha = z\delta\phi$ and again defining the stability boundary at $\sigma_i = 0$

$$real \Rightarrow \frac{\partial \psi}{\partial \phi} + \frac{\partial \psi}{\partial \alpha}z_r = 0 \tag{3.2}$$

$$imaginary \Rightarrow \sigma_r = \frac{U(\lambda n - \frac{\partial \psi}{\partial \alpha}z_i)}{2r + r\mu n} \tag{3.3}$$

basically the same equations as before, except that now for a given z and $\delta\phi$ the required stagger profile is not $z\delta\phi$ as before but $z\delta\phi(\frac{\partial \gamma}{\partial \alpha})$. Letting $\delta\alpha = \sum a_n e^{in(\theta - \sigma t)}$, and $\delta\alpha = z\delta\phi$, the question then becomes once again, for a given z and sensed $\delta\phi$, how do the blades need to be arranged. In other words, what is the relationship, $\frac{\partial \alpha}{\partial \gamma}$, between blade movement and flow angle?

3.2 Calculation of $\frac{\partial \alpha}{\partial \gamma}$

To find an estimate for this term, a potential flow code based on vortex singularity method [10],[22] was written. In this method, the airfoils are replaced by a distribution of a finite number of discrete vortices along the camber line. Use of complex potentials [11] allows straightforward conversion to an infinite 2-D steady cascade, of periodic geometry. The chosen period of this infinate cascade is 0-2π, the unwrapped compressor.

Several basic text books, such as [22],[21] discuss this modeling of airfoils in potential flow fields. The geometry of the airfoil is built up around the camber line. The thickness is added by a distribution of sources and sinks, and the required airfoil circulation is modeled as a vortex sheet along the camber line. Because the thickness distribution does not really affect the flow turning, only thin airfoils are considered. The vortex sheet distribution on each airfoil is found by solving Neuman boundary condition equations of no flux through the airfoil, and satisfying the Kutta condition of $P_u = P_l$, $\gamma_{TE} = 0$, at the trailing edge.

To solve this problem computationally the vortex sheet $\gamma(x)$ is replaced by discrete vortices $\Gamma_i(x_i)$ at specific stations, x_i. $\Gamma_n = 0$ is known from the Kutta condition, but the other n-1 vortex strengths must be determined from the n-1 no flux equations. The points midway between the discrete vortices were choosen as the locations at which to employ the no flux condition. Because the compressor is unwrapped into an infinite cascade of period 2π, the complex potential for an infinite row of vortices of spacing 2π will be used from [11].

$$w = \frac{i\Gamma}{2\pi} \log \sin \frac{\pi z}{a} \tag{3.4}$$

$$u_{induced} = \frac{\Gamma}{2a} \frac{\sin(\frac{2\pi y}{a})}{\cosh(\frac{2\pi x}{a}) - cos(\frac{2\pi y}{a})} = -PGJ(n) \times \Gamma(n) \tag{3.5}$$

$$v_{induced} = -\frac{\Gamma}{2a} \frac{\sinh(\frac{2\pi x}{a})}{\cosh(\frac{2\pi x}{a}) - cos(\frac{2\pi y}{a})} = QGJ(n) \times \Gamma(n) \tag{3.6}$$

where

$$x = x_{source} - x_{field} \quad y = y_{source} - y_{field} \quad a = 2\pi r \tag{3.7}$$

$$PGJ(n) = -\frac{1}{2a}\frac{\sin(\frac{2\pi y}{a})}{\cosh(\frac{2\pi x}{a}) - cos(\frac{2\pi y}{a})} \tag{3.8}$$

$$QGJ(n) = -\frac{1}{2a}\frac{\sinh(\frac{2\pi x}{a})}{\cosh(\frac{2\pi x}{a}) - cos(\frac{2\pi y}{a})} \tag{3.9}$$

The two geometric configurations used were flat plates and circular arcs. Once the misstagger profile has been established, the locations of the discrete vortices, and the no flux control points are all known, and the induced velocity at any point is

$$\vec{V_{induced}} = \sum_{n=1}^{nb\times nvpb} -PGJ(n)\Gamma(n)\vec{i} + QGJ(n)\Gamma(n)\vec{j} \tag{3.10}$$

where n ranges from 1 to nvpb×nb=number of vortices per blade × number of blades. In addition to the induced velocity the freestream velocity is

$$\vec{V_\infty} = V_\infty \cos(\alpha_i)\vec{i} + V_\infty \sin(\alpha_i)\vec{j} \tag{3.11}$$

Hence, the total velocity at a given point is

$$u_{total} = V_\infty \cos(\alpha_i) + u_{induced} \tag{3.12}$$

$$v_{total} = V_\infty \sin(\alpha_i) + v_{induced} \tag{3.13}$$

The no flux equations become $\vec{V_{total}} \cdot \vec{n}$=0 or $\vec{V_{induced}} \cdot \vec{n} = -\vec{V_\infty} \cdot \vec{n}$. This is represented as the matrix equation

$$\begin{bmatrix} \sum_{n=1}^{nb\times nvpb}(-PGJ(n)n_x + QGJ(n)n_y) & & \\ & \cdot & \\ & \cdot & \\ & \cdot & \\ & nb \times nvpb & \end{bmatrix} \begin{bmatrix} \Gamma(n) \\ \cdot \\ \cdot \\ \cdot \end{bmatrix} = \begin{bmatrix} -V_{\infty_n} \\ \cdot \\ \cdot \\ \cdot \end{bmatrix}$$

By leaving $\Gamma(T.E.)$ out of the calculation, it is implicitly set =0 satisfying the Kutta condition. Using a standard gaussian elimination routine on the equation AB=E gives $B = A^{-1}E$. If the vortex strengths are known, the velocity anywhere can be calculated via eqn.(3.12,3.13).

The completed code was checked in several ways, such as fig.(3.1) comparing results for k, (lift on an airfoil in a cascade)/(lift on an isolated airfoil), with Hawthorne [27], calculating flux through the blade, and calculating over a region larger than 360° degrees to check periodicity. Fig.(3.2) shows the basic set up of the cascade, for the particular case of 36 circular arc airfoils at a solidity of 1.8 with mean cascade turning of 10 deg., and 9 moveable blades, misstaggered in a cosine pattern of amplitude $DG_{disc.} = 4°$. The flow angle distribution at .2 chord downstream is also plotted. Flow angle distributions at 1 and .2 chord downstream and the stagger profile of the blades with the mean turning subtracted out are plotted in fig(3.3) for 48 blades, with solidity of 1, and 8 blades moveable. Figure(3.3) graphically illustrates the $\frac{\partial\alpha}{\partial\gamma}$ relationship. Quantitatively this relationship, $\frac{\partial\alpha}{\partial\gamma}$, is the nondimensional magnitude of the created control wave, $\frac{magnitude\ of\ \delta\alpha\ wave}{max.\ amount\ of\ misstagger} = \frac{2a_1}{DG}$. As was done earlier with the stagger profiles, this parameter will also be compared to the continuous, infinite solidity, case giving

$$\frac{\frac{\partial\alpha}{\partial\gamma}_{disc.}}{\frac{\partial\alpha}{\partial\gamma}_{cont.}} = \frac{\partial\alpha}{\partial\gamma} \tag{3.14}$$

since $\frac{\partial\alpha}{\partial\gamma}_{cont.}$=1.

Running the same case as in fig.(2.15) leads to the results of fig.(3.4). This code was then used in a parametric study to investigate the influence of solidity, fraction of blades moved, mean turning of the cascade, and geometry, flat plate vs. circular arcs, on the $a_1 \Leftrightarrow G_1$ relation. Fig.(3.5) summarizes this study showing the effect of these parameters on $\frac{\partial\alpha}{\partial\gamma}$. As expected, $\frac{\partial\alpha}{\partial\gamma}$ approaches 1 as the geometry approaches the continuous case. It is seen that the fraction of blades that are controllable, and the solidity, are far more important than the specific geometry of the blades, such as flat plates, circular arcs, amount of mean turning of the cascade, etc. This is to be expected , since as stated earlier, solidity, and fraction of blades moved are the two parameters that measure how close to the continuous case any other case is.

Figure(3.5) shows that the fraction of blades which are moveable, has the most effect. This point is also made clear by fig.(3.6) which compares moving half of the blades at a given solidity

to moving all of the blades at half that solidity. The fact that $\frac{\partial \alpha}{\partial \gamma}$ actually increased from .416 to .608 shows that increasing the fraction of blades moved more than offsets the loss from decreased solidity. The fixed blades thus attenuate the signal of the moveable ones. It should also be noted that fig. (2.15) is then the inverse of fig.(3.4), as is shown by fig.(3.7), since the ratio of maximum blade misstaggers can be re- written in terms of flow angles using the $\frac{\partial \alpha}{\partial \gamma}$ relationship, giving

$$\frac{DG_{disc.}}{DG_{cont.}} = \frac{(\frac{\partial \gamma}{\partial \alpha}\delta\alpha)_{disc.}}{(\frac{\partial \gamma}{\partial \alpha}\delta\alpha)_{cont.}} = \frac{\partial \gamma}{\partial \alpha_{disc.}} = \frac{1}{\frac{\partial \alpha}{\partial \gamma}_{disc.}} \tag{3.15}$$

with $\delta\alpha_{disc.} = \delta\alpha_{cont.} = z\delta\phi = \delta\alpha_{desired}$ and $\frac{\partial \alpha}{d\gamma}_{cont} = 1$.

The discrepancy in fig.(3.7) is due to the fact that the first analysis had assumed $\frac{\partial \alpha}{d\gamma} = 1$ and in so doing used a control wave of square pulse components, instead of triangular components with $\frac{\partial \alpha}{d\gamma}$ a function of the fraction of blades moved, as in the current analysis. Finally then, with half of the blades moveable $\frac{\partial \alpha}{\partial \gamma}$=.43 from fig.(3.4), and for the example from earlier of a 1% flow perturbation, the maximum blade misstaggering, DG= $\frac{\partial \gamma}{\partial \alpha}\delta\alpha = .5°$. , which is again a reasonable amount of blade turning.

3.3 Choice of Geometry

The final inlet guide vane configuration consisted of 12 NACA .0009, uncambered airfoils, all moveable, at a solidity of .6, equally spaced about the annulus. The geometry of the individual blades was based on the fact that there was not much difference between flat blades and circular arc blades, at least from a control wave launching point of view, fig.(3.5). The overall configuration, solidity, and number of moveable blades resulted from a desire to increase the value of $\phi_{stability\ boundary}$, concerns about separation caused by diffusion in the regions of moveable blades fig.(3.8), and the fact that fixed blades only reduce the fraction of moveable ones, and attenuate the control signal. Experimental testing of the compressor with no inlet guide vanes by Schulmeyer, showed that the reduced solidity would not significantly increase

the stall cell speed, which was roughly 12 Hz. For this geometry, the value of $\frac{\partial \alpha}{\partial \gamma}$, as mentioned before is .608, and the compressor is now on the $\gamma_{igv} = 0°$ speedline. Using this new speedline, and corresponding $\frac{\partial \psi}{\partial \gamma}$ function in the stability analysis developed earlier results in fig(3.9,3.10). From these plots it is seen that for the earlier example the maximum amount of blade deflection required for a 1% disturbance is roughly .36°.

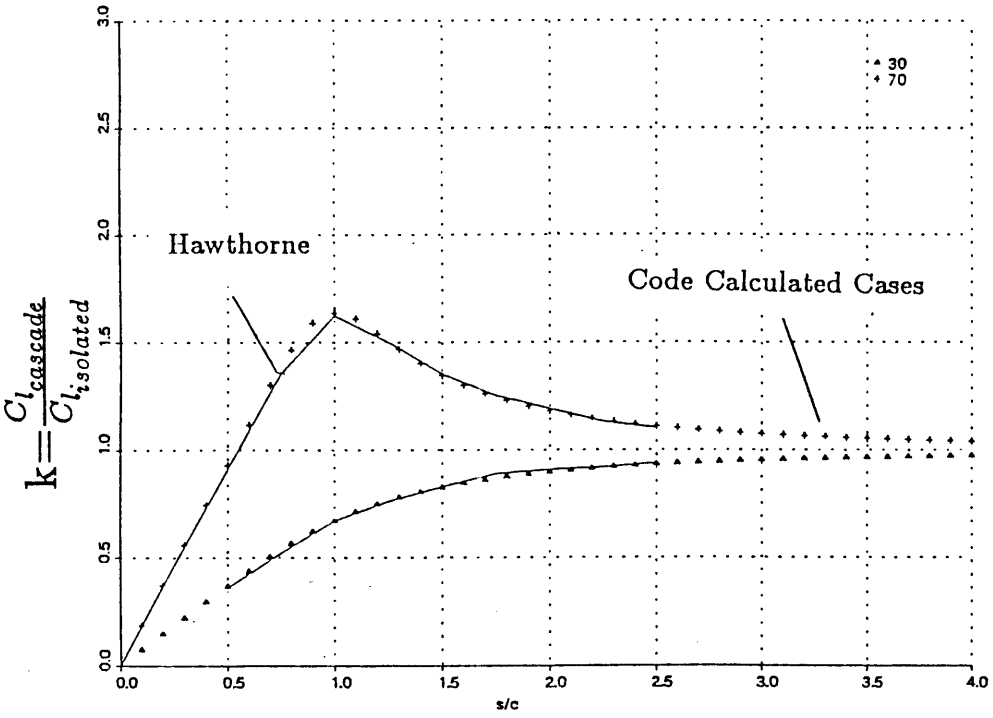

Figure 3.1: Comparrison of results with Hawthorne [27]

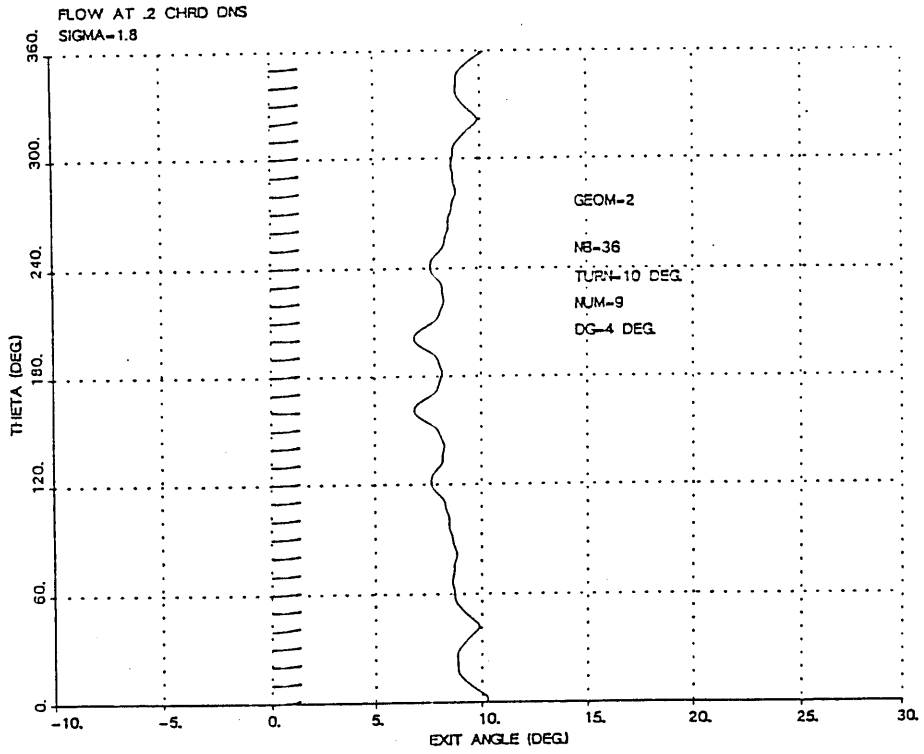

Figure 3.2: Standard cascade arrangement and flow .2 chord downstream, for 36 circular arc airfoils, with a mean cascade turning of 10 deg., and 9 blades mistaggered in a cos. pattern of amplitude $DG_{disc} = 4$ deg.

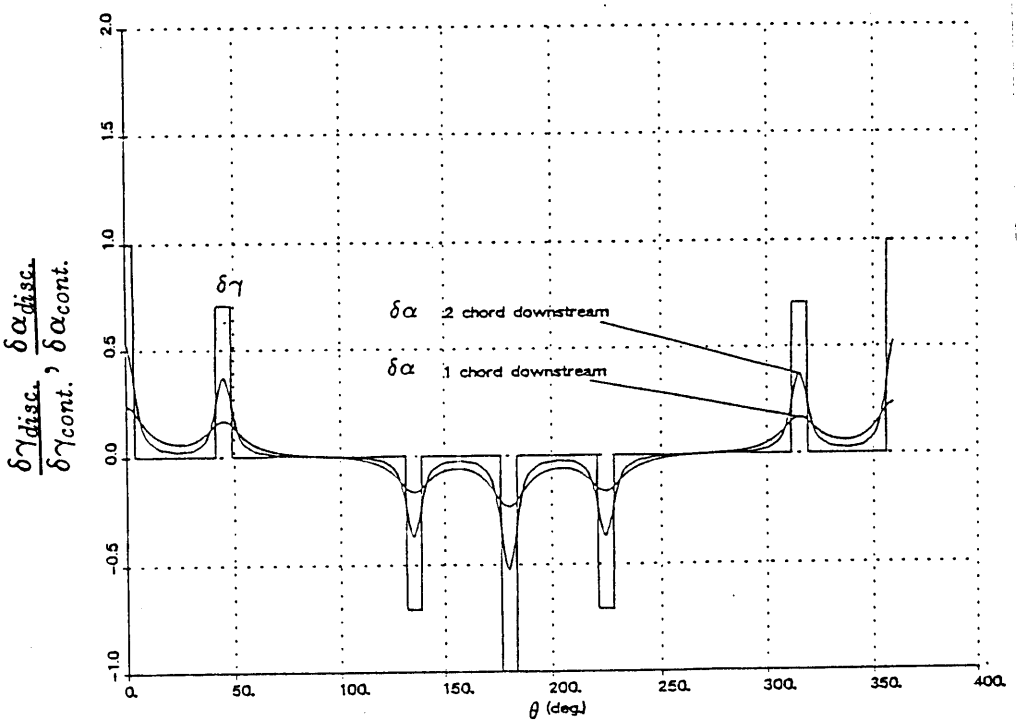

Figure 3.3: 48 blades, 8 moveable, $\sigma = 1.0$ with mean turning subtracted out.

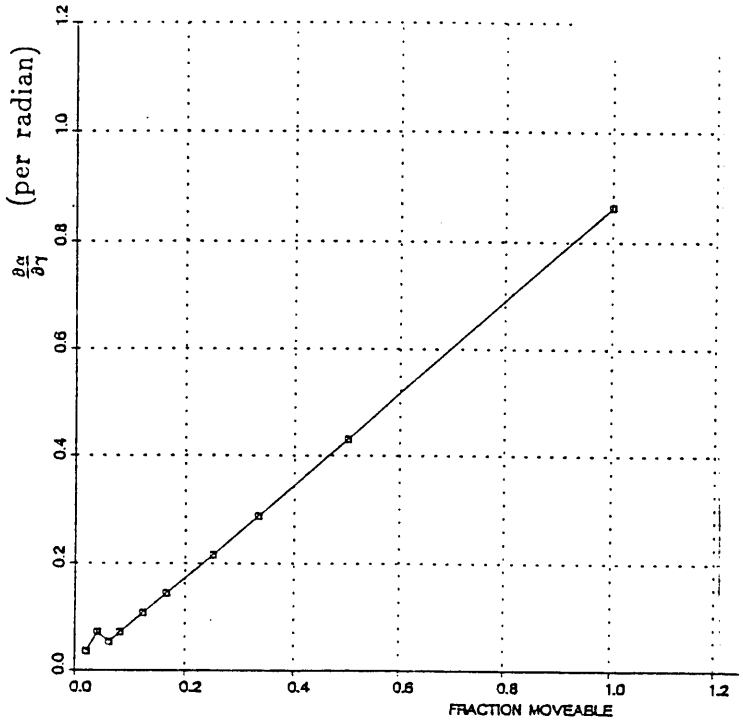

Figure 3.4: $\frac{\partial \alpha}{\partial \gamma}$ vs fraction of blades that are moveable. 48 total blades with $\sigma = 1.0$

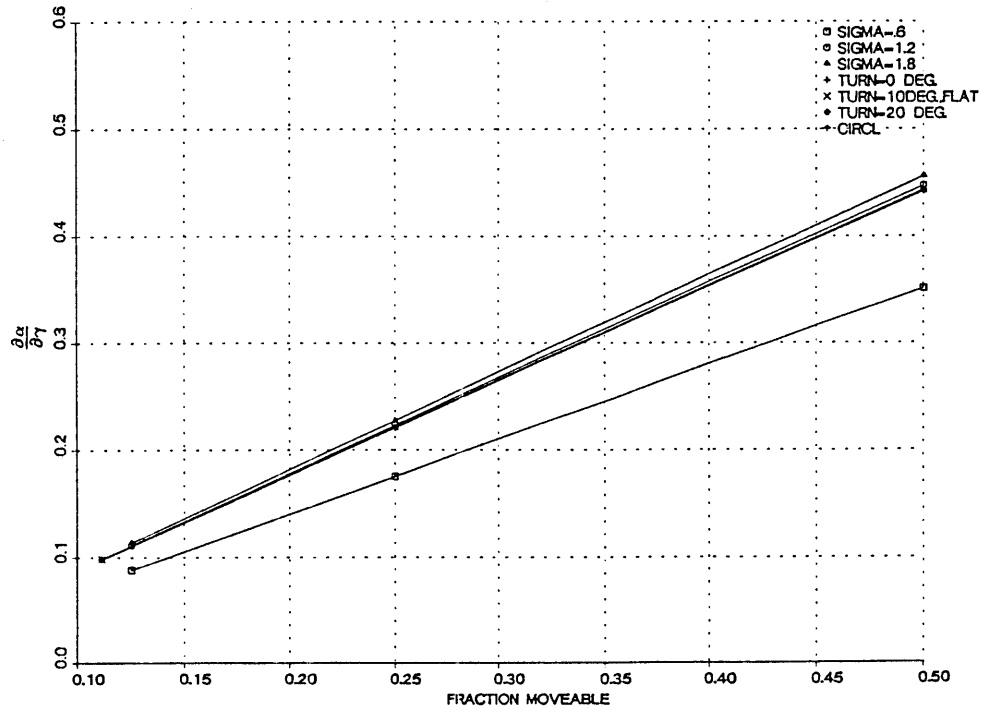

Figure 3.5: Summary of trends
over a portion of the parameter space.

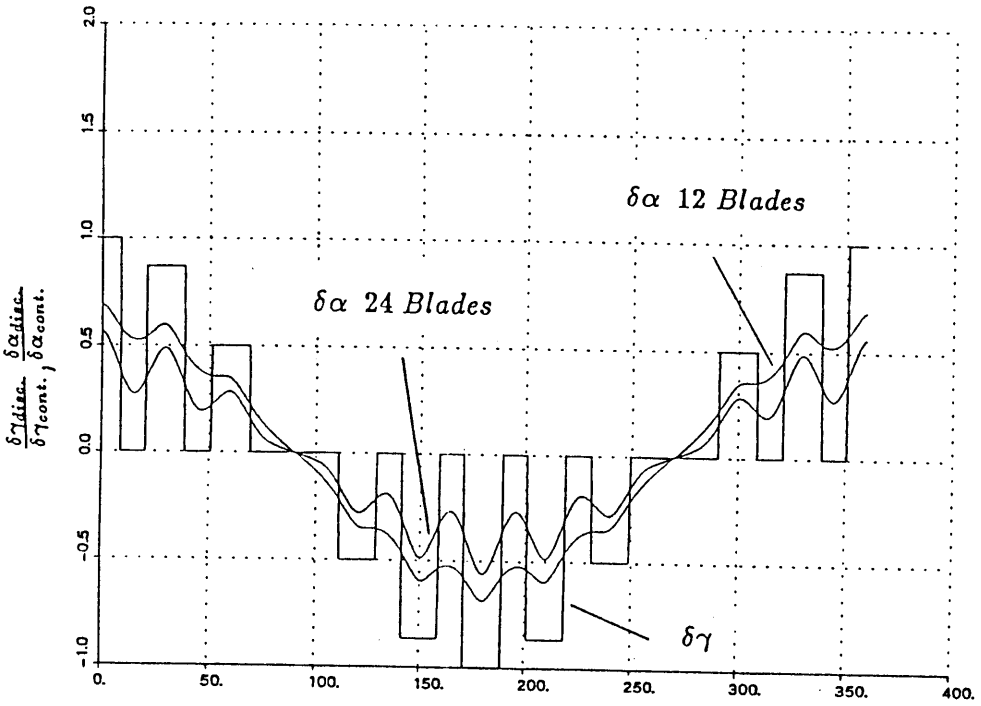

Figure 3.6: Attenuation of control wave by fixed blades, shows that fraction moveable is more important than solidity. Moving 12 of 24 and 12 of 12 total blades.

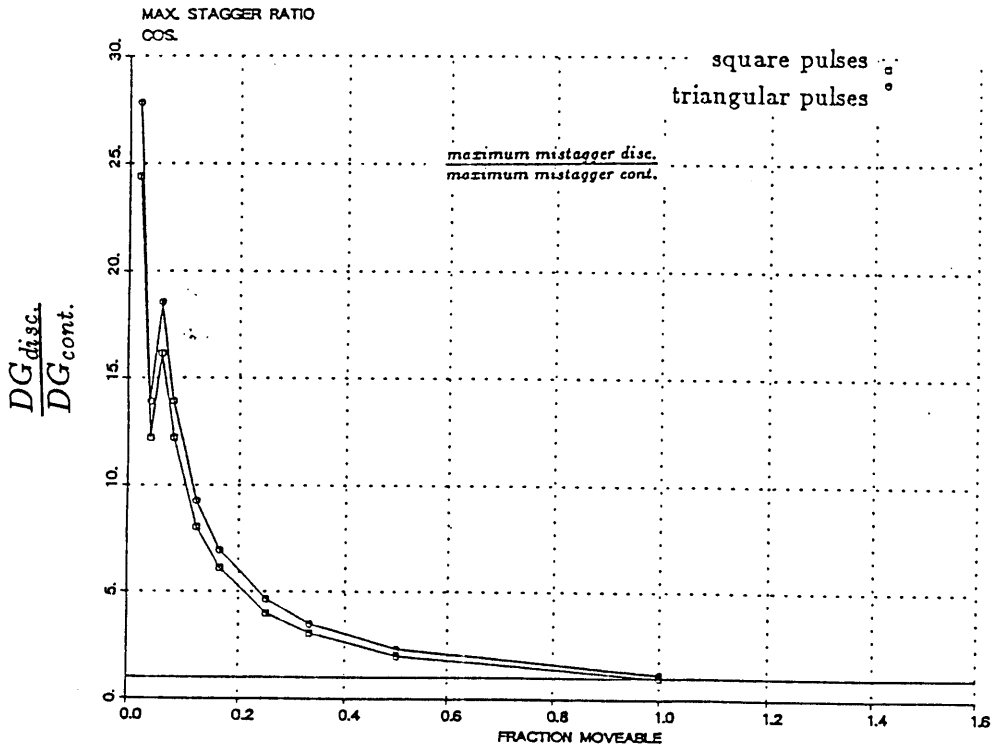

Figure 3.7: Inverse of fig(3.4) compared to fig(2.15)

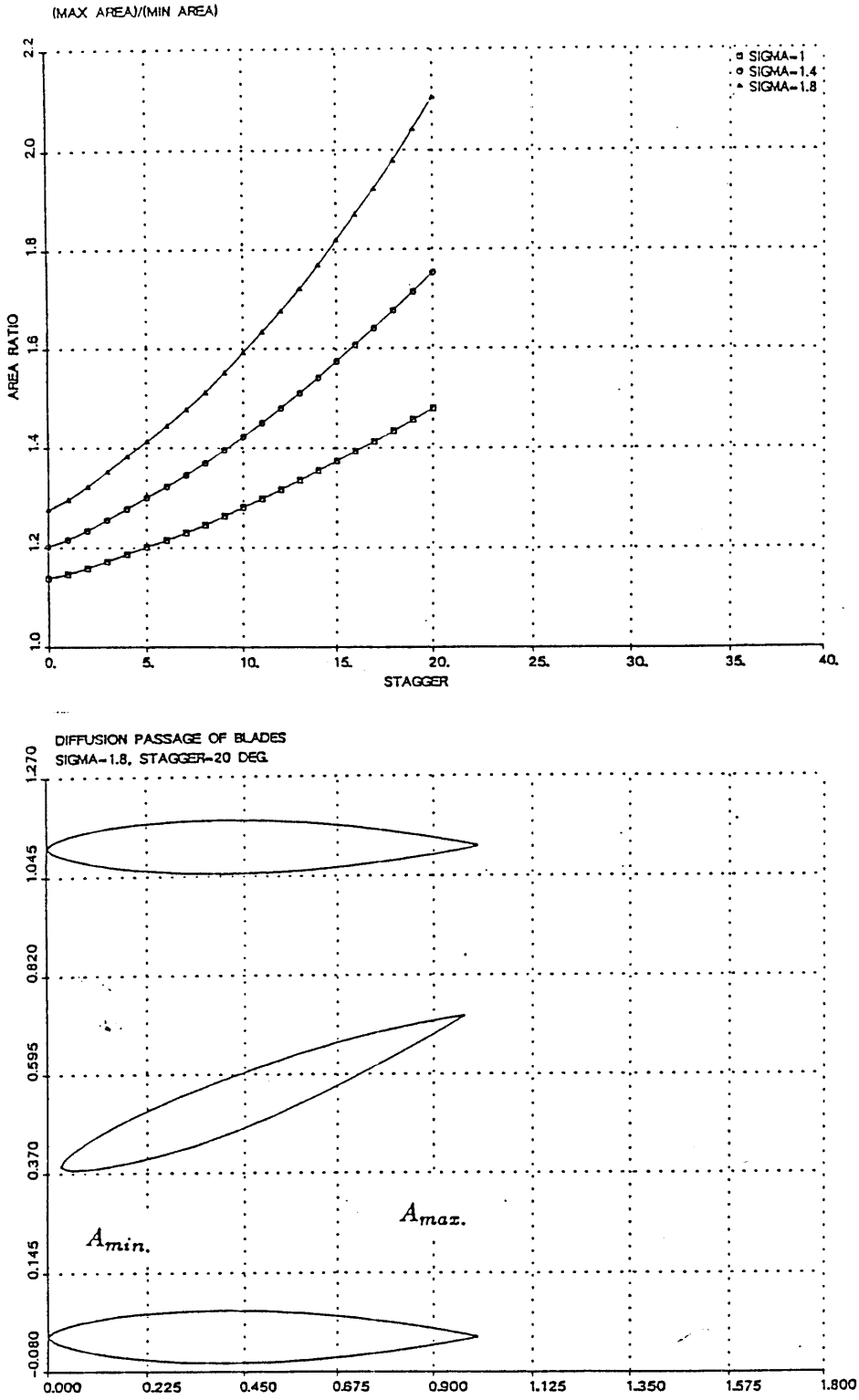

Figure 3.8: Diffusion area ratio $\frac{A_{max.}}{A_{min.}}$ for NACA 0012 blades

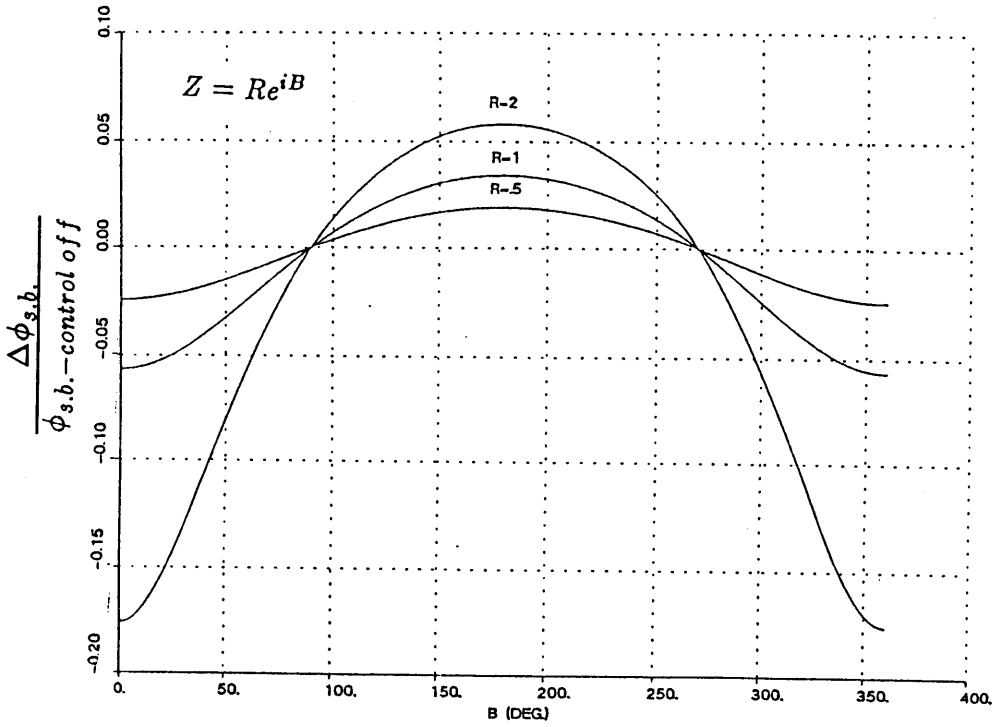

Figure 3.9: Percent change in stability boundary, with R as parameter and $\gamma_{igv} = 0$

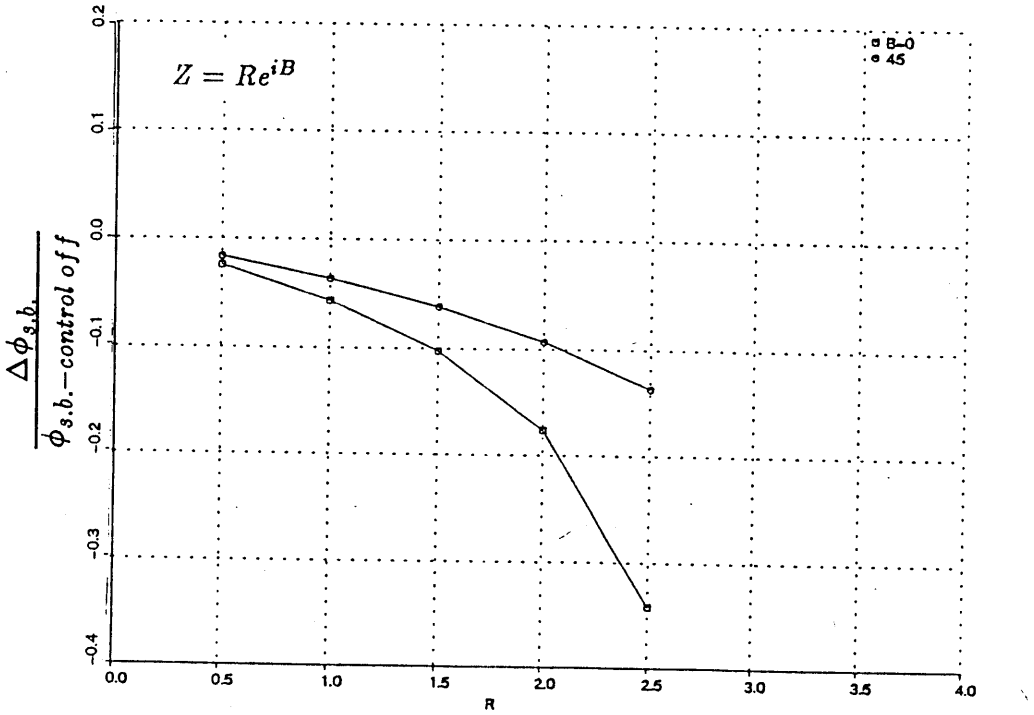

Figure 3.10: Percent change in stability boundary, with B as parameter and $\gamma_{igv} = 0$

Chapter 4

Unsteady Potential Calculations

4.1 Setting up the Equations

To check the final design for reduced frequency effects, a code was written to include unsteadiness from the inlet guide vane motion. The method used was once again a mean camber line point vortex singularity, infinite cascade method based on [8],[9],[10]. However, in this case instead of solving Neuman boundary conditions for the strengths of the vortices, C_p results of the double linearization code by Namba and Toshimitsu [9] were converted into bound vorticity, γ_b. Because the circulation on the airfoils is changing with time, a vortex sheet wake is shed as a consequence of Kelvin's thereom, and must be included in the flow calculations. Following Whithead and Namba [9],[8] the amplitude of vibration is assumed small and the resulting vortex sheet of sinusoidal strength does not distort or curl up, but convects at free stream velocity as a 2-D vortex sheet. This shedding of a vortex sheet is developed by Whithead [8], fig.(4.1), with result

$$bound\ vorticity = \gamma_b(x,t) = \gamma_b e^{i\omega t} \qquad free\ vorticity = \gamma_f(x,t) = \gamma_f e^{i\omega t} \tag{4.1}$$

gives

$$\gamma_f(x) = \frac{-i\omega}{U} \int_{x_{L.E.}}^{x^*} \gamma_b(x_1) e^{\frac{i\omega}{U}(x_1 - x)} dx_1 \tag{4.2}$$

where

$$x^* = x : x_{L.E.} < x < x_{T.E.} \tag{4.3}$$

$$x^* = x_{T.E.} : x_{T.E.} < x$$

and

$$\Delta P(x) = -\rho U \gamma_b(x) \tag{4.4}$$

The Kutta condition is satisfied by having $\gamma_b, \Delta P \rightarrow 0$ at T.E.

The rest of the cascade is created by the time phase shift from blade to blade specified by the interblade phase angle. Therefore, for the infinate cascade of period 12 blades, the inter blade phase angle is 30°. With this geometry and the expressions for all the vorticity γ_b and γ_f the problem can be discretized by letting $\Gamma_i = \gamma_i dx$ and solved in the same method as the steady case, using Lamb's [11] infinite row of vortices potential for both Γ_b and Γ_f . Whereas before, in the steady case, there was only γ_b on the airfoil, now there is γ_b on the airfoils, and γ_f on the airfoil and off of it in the wake. However, in this case, the number of columns of infinite vortices and hence equations is infinite since the wake goes out to infinity. The wake has an asymptotic effect on the flow field, and hence neglecting the wake a relatively far distance away from the calculation point, does not effect the answer, and makes the number of equations finite and the problem solveable.

4.2 Test Comparrisons

Calculations were carried out to check that there was no flux through the blades. Furthermore, wake density, defined as the distance between discrete vortices modelling the continuous sheet, was altered as was wake length, and both had asymptotic effects as expected. As a result of this study, six chord lengths of wake, and a density of a vortex every .1 chord were choosen. Furthermore, the integrated values of C_l and C_m were compared with those of Whitehead [8]. Also, an analytical solution can be obtained for v, the y velocity component at the point (x_0, y_0). Modelling the sinusoidal strength vortex wake as $\gamma sin(x)$ fig.(4.2) then from the potential for a point vortex

$$u_\theta = \frac{\Gamma}{2\pi r} = \int_0^\infty \frac{\gamma sin(x)}{2\pi[(x_0 - x)^2 + (y_0 - y)^2]^{\frac{1}{2}}} dx \tag{4.5}$$

and using angle relations to obtain expressions for the y-cartesian component,

$$v = u_\theta(\frac{x_0 - x}{r}) = \int_0^\infty \frac{\gamma sin(x)}{2\pi r}(\frac{x_0 - x}{r})dx \tag{4.6}$$

at $x_0 = 0$

$$v = -\frac{\gamma}{2\pi}\int_0^\infty \frac{xsin(x)}{r^2}dx = -\frac{\gamma}{4}e^{-y_0} \tag{4.7}$$

Again, results of this calculation exhibited asymptotic behavior with values of $\frac{v_{code} - v_{analytical}}{v_{analytical}}$ of only 2 percent.

4.3 Results

As a final test, calculations of the choosen geometric configuration of 12 blades at a solidity of .6 were done, for the zero and non-zero interblade phase angle cases and checked against the steady code results as reduced frequency approaches 0, fig.(4.3). Once again, the unsteady result $\frac{\partial \alpha}{d\gamma} = .590$ asymptotes to the steady result $\frac{\partial \alpha}{d\gamma} = .608$ as reduced frequency decreases, and the number of vortices per blade increases. Therefore, for the expected reduced frequency of roughly .5, unsteady effects from the blade motion may cause a change in $\frac{\partial \alpha}{d\gamma}$ by a factor of roughly .7, and hence for the 1% disturbance from earlier, the maximum blade deflection becomes .5°.

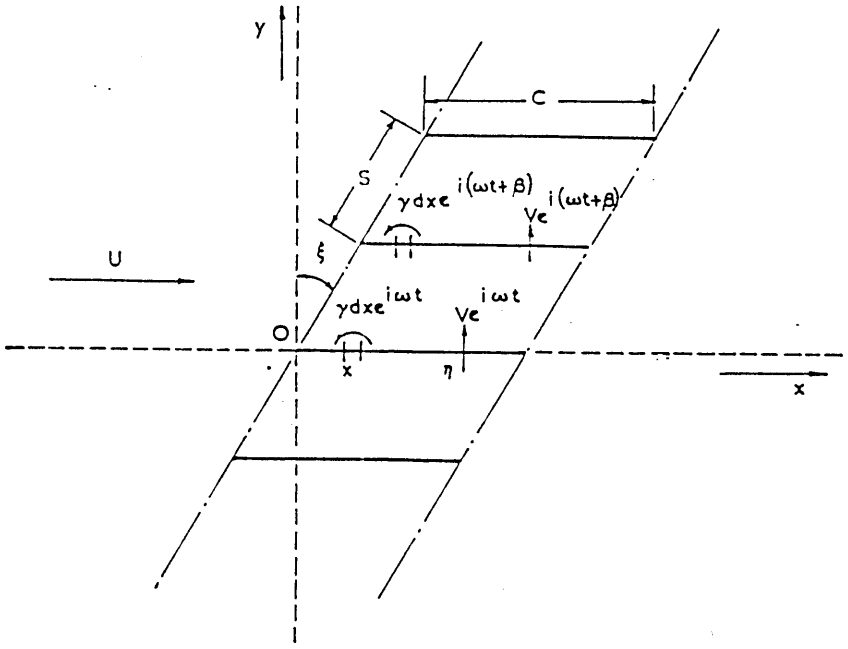

Figure 4.1: Cascade vorticity distribution

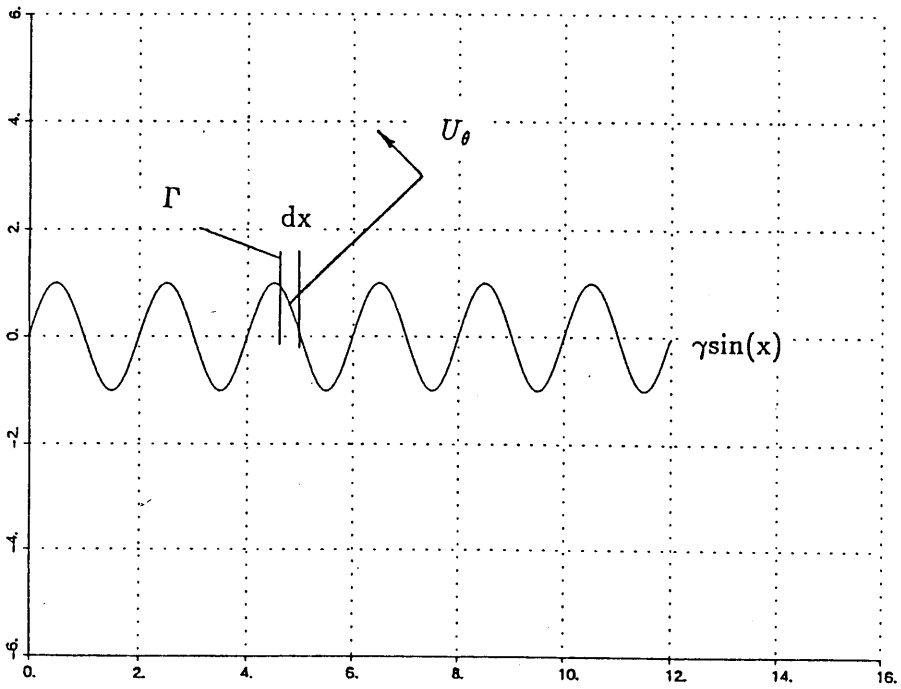

Figure 4.2: Analytical model

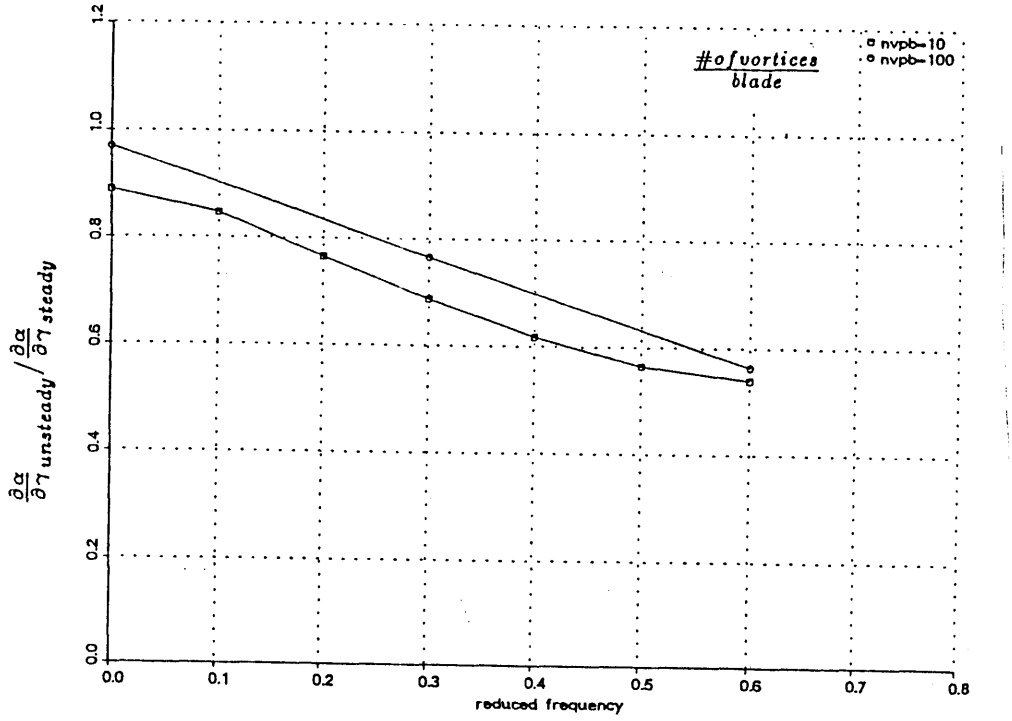

Figure 4.3: Unsteady $\frac{\partial\alpha}{\partial\gamma}$ vs. reduced frequency, asymptoting towards steady value.

Chapter 5

CONCLUSION

5.1 Results

This thesis has been a preliminary investigation into the launching of control perturbations in the compressor via inlet guide vane movement. The fraction of blades that are moveable was found to be the most important parameter governing control wave launching. Solidity was of less importance, with mean turning of the cascade, and camber of the airfoil having an even smaller effect on control wave launching. Several different analytic tools have been developed to show that the maximum blade mistaggering required to create such control perturbations is not prohibitive. All the models show that for 1% flow perturbations, blade movements on the order of only .5° are needed, and initial testing of epoxy blades has acheived this at 100 Hz. In light of these results and those of Garnier [26], for rotating stall precursor sensing, it does seem quite feasible to control rotating stall in its linear perturbation range with moveable inlet guide vanes.

5.2 Future Work

The next locigal step is to actually try to carry out this control on a real machine. Presently, a proof of concept experiment is being assembled at M.I.T. The experiment will be run on the low speed single stage compressor. This machine has an outer diameter of 23.25 in. and an inner diameter of 17.5 in. fig.(5.1). The blading will consist of an inlet guide vane row of 12 blades, the uncambered NACA .0009 airfoils described earlier, 44 rotor blades with solidity of 1.02 and 45 stators with solidity 1.05. The rotor is driven by an electric motor at a range

of speeds 0 - 3000 r.p.m. This is the same compressor used by Garnier [26] and Schulmeyer [20], and further documentation can be found there. A new inlet guide vane ring was designed and built, [29], with provisions for 24 blades, measurement ports, and mounts for actuators and related subsystems fig.(5.2). A full complement of 26 NACA .0009 airfoils were also made. In order to maximize control frequency, and speed for a given actuator, it was desireable to have blades of low moment of inertia. To acheive this, the blades were made out of epoxy cast about a metal spine. The moment of inertia was $I_{zz} = 1.195 \times 10^{-5} kg\ m^2$ (compared to $I_{zz} = 2.933 \times 10^{-5} kg\ m^2$ for solid aluminum [24]). To drive these 12 blades, Paduano [23] has designed a system consisting of 12 Pacific Scientific 4VM62-200-1 D.C. motors with a torque to inertia ratio=$2.67 \times 10^5 s^{-2}$, along with amplifiers, and an air cooling system, all controlled by a 80386 processor. Also in the control loop is a data acquisition system to check flow angles and rates. The locating system for the blade actuators uses optical encoders good to roughly a tenth of a degree. Shake down tests of the motors with the mounted epoxy blades has demonstrated the band width of the servos to be roughly 90Hz. Initial tests will involve measurements of the flowfield downstream of the inlet guide vanes to compare with the predictions of the codes. Stall cell speed will be checked, several speed lines obtained, and finally, control will be attempted by oscillating the blades.

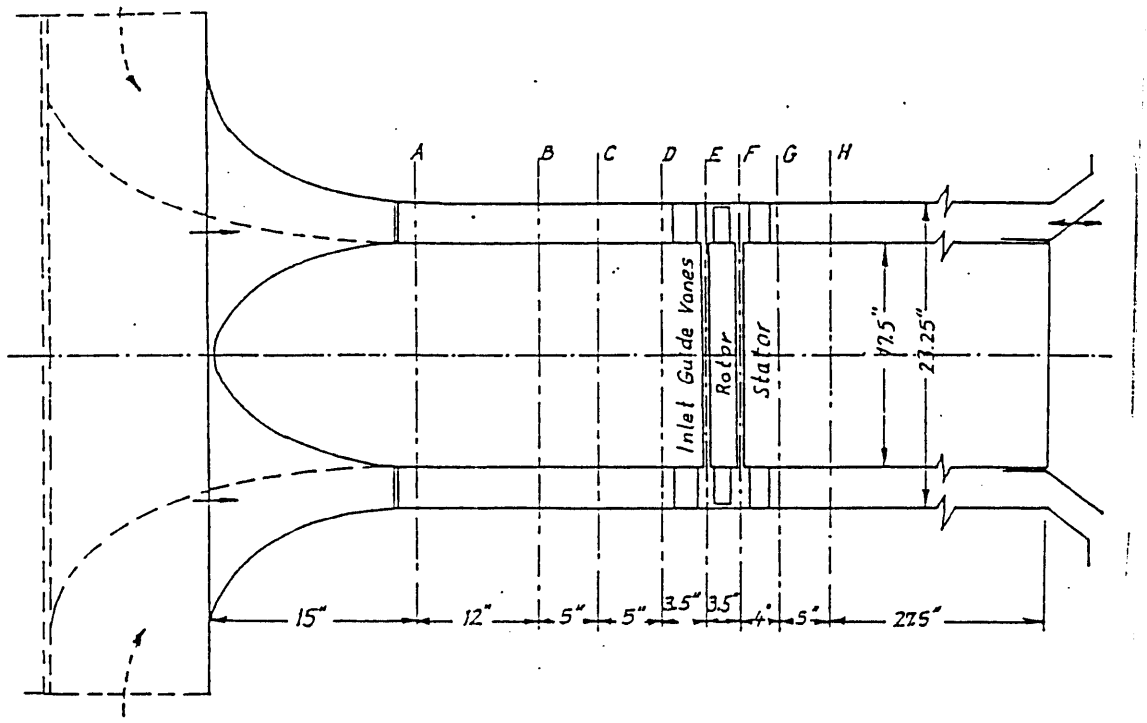

Figure 5.1: Compressor dimensions

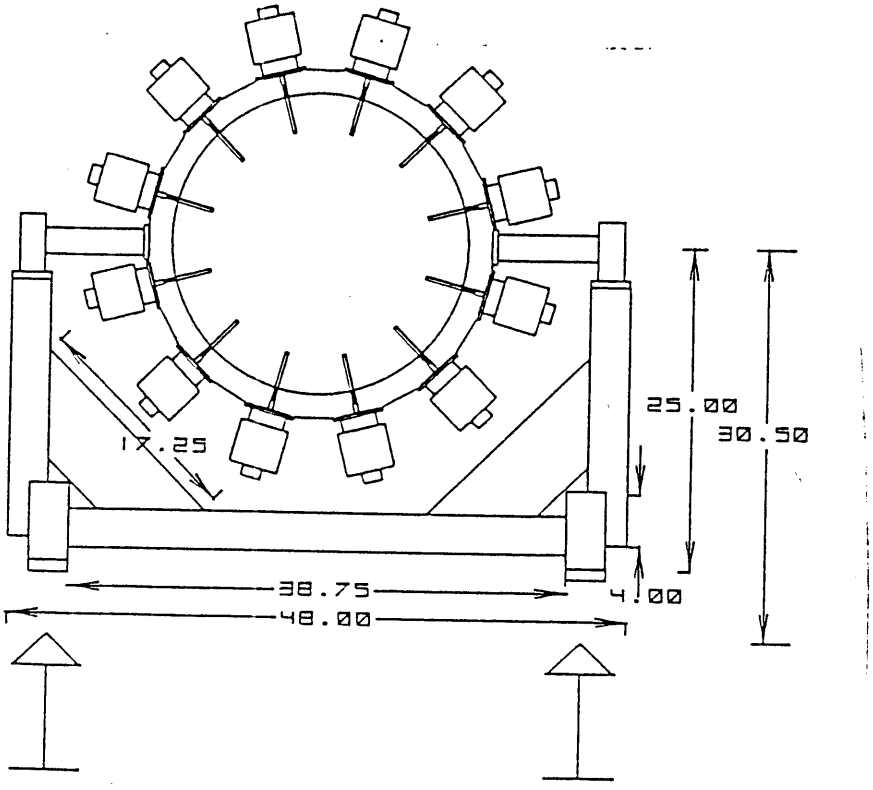

Figure 5.2: Hardware arrangement

Appendix A

Unsteady Potential Calculations

Following the work of Whithead [8], from Kelvin's thereom $\frac{D\Gamma}{Dt} = 0$ so Γ about a curve of fixed identity stays constant, and convects with the fluid. Hence, from fig(A.1) it can be seen that if the bound vorticity, γ_b has changed during the time interval $t_2 - t_1$, the only way for Γ to stay the same is if an element of free vorticity, $\Delta\Gamma_f = -\Delta\Gamma_b$, is formed. Assuming an element of bound vorticity at (x, 0), $\gamma_b = \gamma_b(x)dxe^{i\omega t}$ fig(4.1) where $\gamma_b(x) = \frac{\Gamma_b}{dx} = \Delta u$, this time changing γ_b will lead to a shed vortex sheet of sinusoidal strength fig(4.2). Furthermore, since this vorticity is freely convecting, there is a distinct time, displacement relationship and phase shift.

$$\Delta x = U\Delta t = x_1 - x \tag{A.1}$$

$$\Gamma_f(x_2,t) = \Gamma_f(x_1,t-\Delta t) = \Gamma_f(x_1,t-\frac{\Delta x}{U}) \rightarrow \Gamma_f(x_2)e^{i\omega t} = \Gamma_f(x_1)e^{i\omega(t-\frac{\Delta x}{U})} \tag{A.2}$$

Therefore in relation to $\gamma_b(x)dx$ at (x,0)

$$\Gamma_f(x_1,t) = (constant)e^{i\omega(t-\frac{(x_1-x)}{U})} \tag{A.3}$$

Returning to Kelvin's thereom, in a short time interval δt , the change in Γ_b,

$$\Delta\Gamma_b = \frac{\partial\Gamma_b}{\partial t}\delta t = i\omega\gamma_b(x)dxe^{i\omega t}\delta t \tag{A.4}$$

and since

$$\Delta\Gamma_f = -\Delta\Gamma_b \qquad \Delta\Gamma_f = -i\omega\gamma_b(x)dxe^{i\omega t}\delta t = \Gamma_f \tag{A.5}$$

because $\Gamma_f = 0$ for $t < 0$. This gives the magnitude of the constant in eqn.(A.3). The local sheet strength $\gamma(x_1)$ is distributed over the convected distance

$$U\Delta t = \Delta x \rightarrow \gamma_f(x_1,t) = \frac{\Delta\Gamma_f}{U\Delta T} = \frac{-i\omega}{U}\gamma_b(x)dxe^{i\omega(t-\frac{\Delta x}{U})} \tag{A.6}$$

To obtain the complete value of γ_f the contributions form all the other $\gamma_b dx$ must be included.

$$\gamma_f(x_1,t) = \frac{-i\omega}{U}\int_0^{x_1} \gamma_b(x)dx e^{i\omega(t-\frac{\Delta x}{U})} \tag{A.7}$$

Letting

$$\gamma_b(x,t) = \gamma_b e^{i\omega t} \qquad \gamma_f(x,t) = \gamma_f e^{i\omega t} \tag{A.8}$$

gives

$$\gamma_f(x) = \frac{-i\omega}{U}\int_{x_{L.E.}}^{x^*} \gamma_b(x_1) e^{\frac{i\omega}{U}(x_1-x)} dx_1 \tag{A.9}$$

where

$$x^* = x : x_{L.E.} < x < x_{T.E.} \tag{A.10}$$

$$x^* = x_{T.E.} : x_{T.E.} < x$$

A differentil equation relating γ_b and γ_f can be obtained by differentiating (A.9) with respect to x over the blade surface, using Leibinitz's rule

$$\frac{\partial \gamma_f}{\partial x} + \frac{i\omega}{U}(\gamma_f + \gamma_b) = 0 \tag{A.11}$$

By applying the linearized Euler equation on both the upper and lower surfaces of the airfoil

$$(\frac{\partial}{\partial t} + U\frac{\partial}{\partial x})(ue^{i\omega t}) = -\frac{1}{\rho}\frac{\partial P}{\partial x}e^{i\omega t} \tag{A.12}$$

$$(\frac{\partial}{\partial t} + U\frac{\partial}{\partial x})[(u_l - u_u)e^{i\omega t}] = -\frac{1}{\rho}\frac{\partial (P_l - P_u)}{\partial x}e^{i\omega t} \tag{A.13}$$

remembering that $\Delta u = \gamma_{total} = \gamma_f + \gamma_b$

$$(\frac{\partial}{\partial t} + U\frac{\partial}{\partial x})(\gamma_f + \gamma_b) = -\frac{1}{\rho}\frac{\partial \Delta P}{\partial x} \tag{A.14}$$

$$i\omega(\gamma_f + \gamma_b) + U\frac{\partial \gamma_b}{\partial x} + U\frac{\partial \gamma_f}{\partial x} = -\frac{1}{\rho}\frac{\partial \Delta P}{\partial x} \tag{A.15}$$

and using equation (A.11) gives.

$$i\omega(\gamma_f + \gamma_b) = -U\frac{\partial \gamma_f}{\partial x} \Rightarrow U\frac{\partial \gamma_b}{\partial x} = -\frac{1}{\rho}\frac{\partial \Delta P}{\partial x} \tag{A.16}$$

Integrating this equation with one of the limits off of the airfoil, and using the fact that $\Delta P = \gamma_b = 0$ off of the airfoil gives

$$U\gamma_b = -\frac{1}{\rho}\Delta P \rightarrow \Delta P(x) = -\rho U \gamma_b(x) \tag{A.17}$$

The Kutta condition is satisfied by having $\gamma_b, \Delta P \rightarrow 0$ at T.E.

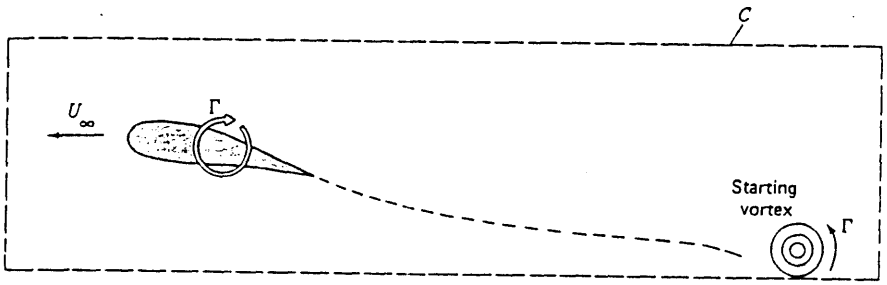

Figure A.1: Shed vortex for Kelvin's thereom [21]

Bibliography

[1] Hynes, T.P. and Greitzer, E.M., "A Method for Assessing Effects of Circumferential Flow Distortion on Compressor Stability," Journal of Turbomachinery, Vol. 109, July 1987, pp.371-379.

[2] Greitzer, E.M., "Review-Axial Compressor Stall Phenomena," ASME J. of Fluids Engineering, Vol. 102, June 1980, pp. 134-151.

[3] Emmons, A.W., C.E. pearson, and H.P. Grant, "Compressor Surge and Stall Propagation," Trans. ASME, Vol. 79 , April 1955, pp. 455-469.

[4] Epstein, A.H., Ffowcs Williams, J.E., and Greitzer, E .M., "Active Suppression of Compressor Instabilities," AIAA-86-1994, AIAA 10th Aeroacoustics Conference, July, 1986.

[5] Moore, F.K. and E.M. Greitzer, "A Theory of Post-Stall Transients in Axial Compression Systems: Part I-Development of Equation," ASME J. Eng. for Power, Vol. 108, January 1986, pp. 68-76.

[6] Greitzer, E.M., "A Note on Compressor Exit Static Pressure Maldistributions in Asymmetric Flow," CUED/A-Turbo/TR 79, 1976.

[7] G.T. Chen, E.M. Greitzer, and A.H. Epstein, "Enhancing Compressor Distortion Tolerance By Asymmetric Stator Coontrol," AIAA-87- 2093, AIAA/SAE/ASME/ASEE 23rd Joint Propulsion Conference, July, 1987

[8] Whitehead, D.S., "Force and Moment Coefficients for Vibrating Aerofoils in Cascade," Reports and Memoranda No. 3254, Ministry of Aviation, England, Feb. 1960.

[9] Namba, M., and Toshimitsu, K., "Improved Double Linearization Method For Prediction Of Mean Loading Effects on Subsonic and Supersonic Cascade Flutter"

[10] Barber, T.J., and Weingold, H.D., "Vibratory Forcing Functions Produced by Nonuniform Cascades," Engineering For Power, Transactions of the ASME, Vol. 100, January 1978, pp.82-88.

[11] Lamb, H., Hydrodynamics, Dover Press, New York, 1945, p. 71.

[12] Raw, J.A., and Weir, G.C., "The Prediction of Off-Design Characteristics of Axial and Axial/Centrifugal Compressors," SAE 800628, Turbine Powered Executive Aircraft Meeting, April, 1980

[13] Moore, F. K., "A Theory of Rotating Stall of Multistage Compressors, Part I,II,III," ASME Journal of Engineering For Power, Vol. 106, No. 2, Apr. 1984, pp. 313-336.

[14] Plourde, G., and Stenning, A., "Attenuation of Circumferential Inlet Distortion in Multistage Compressors," AIAA Paper 67-415, Aug. 1967.

[15] Stenning, A. H., "Inlet Distortion Effects in Axial Compressors", Journal of Fluid Engineering, Vol. 102, March 1980.

[16] Mazzaway, R. S., "Multiple Segment Parallel Compressor Model for Circumferential Flow Distortion", Engineering for Power, Vol. 99 No. 2, April 1977.

[17] Stenning, A. H., "Rotating Stall and Surge", Journal of Fluid Engineering, Vol. 102, March 1980.

[18] Pinsley, J.E., "Active Control of Centrifugal Compressor Surge", M.S. Thesis, Department of Aeronautics and Astronautics, MIT, Oct. 1988.

[19] Gysling, D.L., "Dynamic Control of Centrifugal Compressor Surge Using Tailored Structure", M.S. Thesis, Department of Aeronautics and Astronautics, MIT, Oct. 1988.

[20] Schulmeyer, A., "Enhanced Compressor Distortion Tolerance Using Asymmetric Inlet Guide Vane Stagger", M.S. Thesis, Department of Aeronautics and Astronautics, MIT, Oct. 1988.

[21] Potter, M.,C., Foss, J.,F., Fluid Mechanics, Great Lakes press, inc., Okemos, MI,1982.

[22] Kuethe, A.,M., Chow, Y.,C., Foundations of Aerodynamics, Wiley, New York, New York, 1986.

[23] J. Paduano, personal communication, 1989.

[24] J. Guenette, personal communication, 1989.

[25] M. Drela, personal communication, 1989.

[26] Garnier, V., "Experimental Investigation of Rotating Waves as a Rotating Inception Indication in Compressors", M.S. Thesis, Department of Aeronautics and Astronautics, MIT, June 1989.

[27] "Volume X High Speed Aerodynamics and Jet Propulsion",
Aerodynamics of Turbines and Compressors,
Hawthorne W.,R., editor, Princeton University press, Princeton, New Jersey 1964.

[28] Kerrebrock, J.,L., Aircraft Engines and Gas Turbines, The MIT Press, Cambridge, MA., 1984.

[29] A. Epstein, personal communication, 1989.